

SBIR A02.07: VTOL to Transonic Aircraft

Final Technical Report
July 24, 2006

Acuity Technologies Inc.
Principal Investigator: Robert Clark
3475 Edison Way Unit P
Menlo Park, CA 94025
650-369-6783

Issued by

NASA Dryden Flight Research Center
PO Box 273, Mailstop 1422
Edwards, California 93523-0273
Attn: Michelle L. Vial, (661) 276-3513

Contract No. NND06AA26C
Effective Date: 1/26/2006

Technical Liaison
Richard Maine
661-276-3316
Richard.Maine@nasa.gov

SBIR Rights Notice (Mar 1994)

These SBIR data are furnished with SBIR rights under Contract No. NND06AA26C. For a period of 4 years after acceptance of all items to be delivered under this contract, the Government agrees to use these data for Government purposes only, and they shall not be disclosed outside the Government (including disclosure for procurement purposes) during such period without permission of the Contractor, except that, subject to the foregoing use and disclosure prohibitions, such data may be disclosed for use by support Contractors. After the aforesaid 4-year period the Government has a royalty-free license to use, and to authorize others to use on its behalf, these data for Government purposes, but is relieved of all disclosure prohibitions and assumes no liability for unauthorized use of these data by third parties. This Notice shall be affixed to any reproductions of these data, in whole or in part.”

The views and conclusions contained in this document are those of the authors and should not be interpreted as representing the official policies, either express or implied, of NASA or the U.S. Government. Distribution limited to U.S. Government agencies only.

Destroy by any means which prevents reproduction of this document.

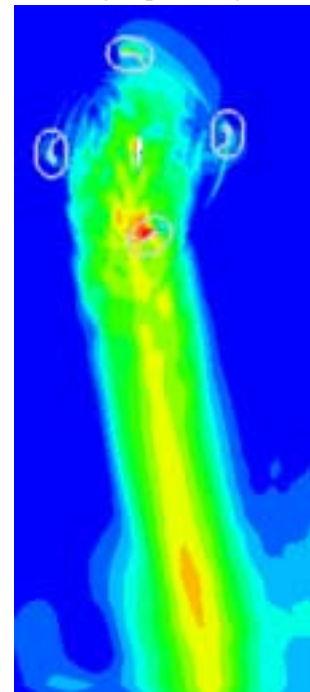
VTOL to Transonic Aircraft Project Summary

The cyclogyro, an aircraft propulsion concept with the potential for VTOL to the lower bounds of transonic flight, is conceptually simple but structurally and aerodynamically complex. To our knowledge no cyclogyro has ever flown. We have demonstrated through simulation and rotor testing that with appropriately designed cyclogyro rotors and propulsion algorithms, aircraft can transition smoothly from low-speed and vertical flight to near-transonic forward flight.



The cyclogyro is one of the most heavily studied subsonic aircraft concepts that has never flown. It is based on the principle that airfoils arranged with their spans parallel to an axis of powered rotation normal to aircraft direction of flight can be controlled in pitch so as to provide lift and/or thrust in any direction within a vertical plane, as shown above. This is not a new concept, and its potential for VTOL to high speed flight has long been recognized.

In our Phase I work we have demonstrated through CFD simulations and through construction and tests of a working cyclogyro rotor that cycloidal drive can be an effective, practical aircraft lift and propulsion technique. We have obtained lift to power ratios as good as those for modern helicopters at matching area loading.



The results of our work clearly show the potential and practicality of cycloidal propulsion. Continuation of this work through Phase 2 will result in construction of a flying cyclogyro controlled by a ground-based pilot, and initiation of manned prototype design. Cyclogyro applications include convenient commercial transportation, rapid disaster/rescue response, and flexible multi-mission defense vehicles with higher speed, lower noise, and better safety than today's rotorcraft.

1 Table of Contents

1	Table of Contents	3
2	Identification and Significance of the Innovation	5
2.1	Program Tasks	5
	Cyclogyro History	6
	Rotor Flight Modes	7
	The Challenge and Opportunity	8
3	Phase I Technical Objectives	8
4	Phase I Work Plan	9
4.1	Task 1. Rotor Simulation	9
4.1.1	Work to Date	9
	Simulation Conditions	9
	Simulation Results	10
4.2	Task 2. Blade Weight, Loads and Bending	17
4.3	Task 3: Phase 1 Rotor Blade Construction	19
4.4	Task 4: Rotor Design and Fabrication	20
4.4.1	Blade Control Concepts	20
4.4.2	Task 5: Static Testing	21
4.5	Phase I Schedule	21
5	Potential Applications	21
5.1	Potential NASA Commercial Applications	21
5.2	Potential Non-NASA NASA Commercial Applications	21
6	Contacts	21
6.1	Key Contractor Participants	21
6.2	Key NASA Participants	22
6.3	NASA and Non-NASA Advisors	22
7	Technical Activities	22
7.1	Cumulative Technical Activities	22
7.1.1	Phase I Technical Accomplishments	22
7.1.2	Design Changes	23
7.1.3	Blade Airfoil Design	23
7.1.4	CFD Work	24
7.1.4.1	An Overview of Overflow 2	25
7.1.4.1.1	Structured Grids, Boundary Conditions and X-ray cutting	25
7.1.4.1.2	Moving Grids in Overflow	26
7.1.4.2	CFD Results	26
7.1.4.2.1	CFD Setup and Parameters	26
7.1.4.2.2	Graphical Summary	27
7.1.4.3	FOMOCO Results	32
7.1.4.3.1	Force Superposition and Blade Profile Optimization	33
7.1.4.3.2	Forward Flight	38
7.1.5	Rotor and Test Stand Model	41
7.1.5.1	Rotor Supports and Lift/Thrust Load Cells	43
7.1.6	Test Instrumentation and Parameter Measurement	45
7.1.7	Test Results	46
7.1.7.1	Rotor RPM and Motor Torque	47

7.1.7.2	Blade Tension	48
7.1.7.3	Lifting Forces.....	48
7.1.7.4	Parasitic Drag Determination: Fixed Angle Runs.....	49
7.1.8	Blade Forces	50
7.1.9	Results of Lift Measurement Runs	52
7.1.9.1	Lift to Power Ratio	53
7.1.9.2	Blade Angle Servo Accuracy.....	54
7.1.9.3	Performance At Two Speed Points	55
7.1.9.4	Blade Angle Precompensation at High Speed	55
7.1.9.5	Maximum Speed Reached	57
7.1.9.6	Discussion	58
7.1.9.7	Power lost to Parasitic Drag.....	58
7.1.9.8	Estimation of Higher Speed Performance.....	58
7.1.9.9	Full Size Rotor Performance.....	59
7.1.9.10	Parts Drawings.....	61
7.1.9.11	Conclusions from Test Results	61
7.2	Future Technical Activities	61
8	Potential Customer and Commercialization Activities	62
8.1	Cumulative NASA Potential Customer Activities	62
8.2	Cumulative Non-NASA Potential Customer Activities	62
8.3	Other Cumulative Commercialization Activities	63
9	Resources Status	63
	References.....	64
	Parts Drawings.....	65

2 Identification and Significance of the Innovation

(The following is extracted from our phase 1 proposal.)

The cyclogyro is one of the most heavily studied subsonic aircraft concepts that has never flown. It is based on the principle that airfoils arranged with their spans parallel to an axis of powered rotation normal to aircraft direction of flight can be controlled in pitch so as to provide lift and/or thrust in any direction within a vertical plane, as shown in Figure 1. This is not a new concept, and its potential for VTOL to high speed flight has long been recognized[1][2][9]. NACA cyclogyro theoretical work and rotor wind tunnel tests from 1931 through 1935 concluded that the concept was valid, but power requirements rendered the cyclogyro impractical. However, vertical lift power requirements were comparable to those of modern helicopters, and apparently the possibility that the rotor blades could rotate at low speeds relative to the aircraft forward airspeed was not considered.

There are several potential performance advantages of the cyclogyro over conventional VTOL and fixed wing aircraft. The use of common surfaces for lift and thrust across all flight speeds offers efficiency in the elimination of wing drag at high speed. The rotary blade motion about a transverse aircraft axis provides the opportunity to produce lift and thrust while the blades are moving backward relative to the aircraft, which allows high intermittent blade C_L for lift and thrust near transonic aircraft speeds. Rotor speed and pitch need not increase with airspeed, and Acuity's simulations show that attainable thrust increases with forward airspeed at constant rotor rotation rate. Rotor lifting area, and therefore VTOL efficiency, falls between helicopters and direct jet vectored thrust.

The benefits of a VTOL capable craft that can approach the speed of sound in forward flight without radical reconfiguration are many, including convenient commercial transportation, rapid disaster/rescue response, and flexible multi-mission defense vehicles. We propose that the realization of a successful cyclogyro design can be accomplished with revolutionary structural and aerodynamic innovations, and a successful cyclogyro would be a revolutionary subsonic aircraft.

A practical cyclogyro would provide a NASA with a versatile, capable observation platform, chase plane, and instructional aeronautics demonstrator, as well as a test vehicle for improving cyclogyro flight characteristics and efficiency.

We propose that if cyclogyro blades are symmetric and controllable through unlimited pitch relative to the supporting rotor structure, the aircraft can transition smoothly from low-speed and vertical flight to high-speed forward flight by slowing the rotor so that the blade rotational speed drops below the forward airspeed. As we show below, thrust and lift can be maintained across all speeds, and attainable thrust increases with increasing airspeed for constant rotor speed.

2.1 Program Tasks

(The following is extracted from our phase 1 proposal.)

In Phase 1 we propose to study and simulate rotors and rotor control hardware and software, build working rotors using design and construction techniques enabling extremely stiff lightweight structures and high speed control of lifting surfaces, and to static test them to verify predicted performance.

We will construct prototype blades with a carbon fiber and fiberglass skin of varying skin thickness to provide uniform bending stiffness in all directions in the airfoil to allow low-force control of angle of attack of a bending blade. In high speed flight, our design reduces rotation induced force by biasing the

blade angle of attack radially inward. Blade stiffness to weight and blade length will be chosen such that resonances are avoided or managed.

Finally, we will design and test a rotor using the blades constructed, to verify rotor performance in static conditions. A mechanism for implementing a wide range of rotor blade incidence profiles is outlined below, and the mechanical components for this will be designed and built. These will be assembled with an electric motor, rotary strain gauge coupling, and the blades to measure power and static lift and compare results with phase 1 performance predictions. .

In Phase 2 we will first incorporate the rotors into a flying small scale aircraft, and fly it using conventional radio control/UAV airplane and helicopter control and stabilization technology. We will demonstrate that the design concept is practical for speed ranges from hover to high-speed forward flight at speeds well above those attainable by helicopters. In this we will address many of the practical aspects of cyclogyro implementation and will permit further exploration of the potential of cyclogyros for flight from VTOL to fixed-wing critical mach airspeeds.

In phase 2 we will also build and test wind tunnel models of rotors across subsonic flight regimes to identify the limit of forward flight speeds. We will initiate relationships with aircraft developers and with investors to design, study and test a full scale prototype in phase III. Finally, we will proceed with design of a full scale cyclogyro.

Cyclogyro History

Perhaps the earliest attempt at cyclogyro construction is illustrated in Figure 2a, a 1930 photograph of an aircraft built by E. A. Schroeder based in San Francisco, that would have used the cyclogyro blades only for propulsion. Figure 2b is a cyclogyro built by Rahn Aircraft in 1935. Apparently neither these nor any other cyclogyros have ever flown.



Figure 2a. Schroeder Cyclogyro



Figure 2b. Rahn Cyclogyro

In 1935 the challenges of building a working cyclogyro proved insurmountable. However, the theoretical and experimental power/lift ratios obtained were similar to those required for hover in modern helicopters[3][4] at 0.1 to 0.15 hp/lb. The hover power required of 150% of power at minimum power cruise speed matches the power required for modern helicopters very closely, as shown in the power required vs. airspeed curves for the AH-64 Apache in Figure 5.

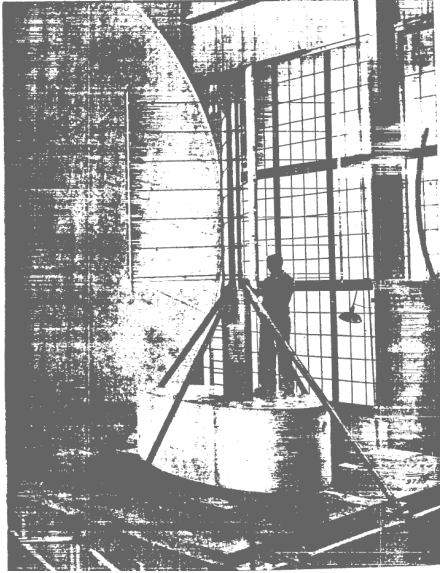


Figure 3a. NACA Rotor Tested

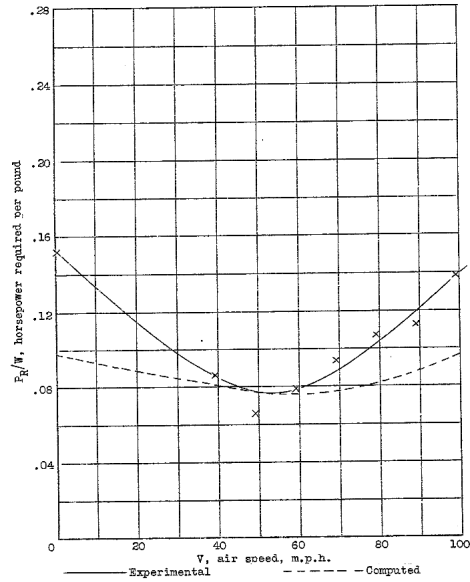


Figure 18.-Cyclogyro performance calculation.

Figure 3b. NACA Power/Thrust Theory & Results

After this concentrated activity in the 1930s, cyclogyro development was quiescent until the 1980s. Since then several vertical axis, or Darrieus, windmills have been constructed which successfully use a constant-pitch version of the cyclogyro principle for power generation[5], and cyclogyro lift and propulsion was considered for hybrid heavy lift systems[6].

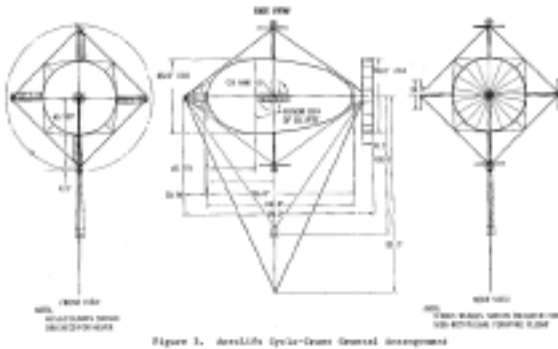


Figure 4a AeroLift Cyclo-Crane Concept, c.1980



Figure 4b. Three Vertical Axis Windmills

In 1993 a patent to Northrop covering a particular method of blade pitch control was issued. Other recent activity in cyclogyros includes U.S. Patent 6,932,296 issued August 23, 2005 for a control system of a cycloidal UAV (although not to Acuity), which discusses the modes in which a cyclogyro rotor could operate.

Rotor Flight Modes

The limitations of critical Mach on advancing blades and retreating blade stall hold the maximum possible forward speed of helicopters to around 200 knots. The V-22 and other experimental aircraft have attempted to overcome this, with limited success. Ducted fan blades have constraints similar, although less stringent, to those on helicopter blades, again limiting forward speed. Ducted fan and direct jet powered VTOL aircraft are inefficient at low speeds due to high exit velocities and limited area lifting discs.

The proposed design has the potential to overcome these limitations. Blade rotation speeds can be much lower than the craft airspeed, allowing generation of lift and thrust close to critical Mach for a fixed wing. Figure 1 suggests the use of turbojets or turbofans to power cyclogyro rotors. If these engines transition during flight to provide aircraft thrust at high speed, the rotors can be stopped and the blades used as fixed wings.

In hover or low speed flight, the rotors blade airspeed would be higher than the aircraft airspeed, and the blades would vary their angle of attack around a direction aligned with the rotor circumference. As was show below, as aircraft speed increases the rotor speed can remain constant. Receding blade stall is much less serious than in a helicopter as it occurs equally along blades, and first occurs at the aircraft longitudinal center of lift, thus no rolling or pitching is induced. In any event the active control of the blades would be programmed to keep the angle of attack below stall.

When the retreating blade airspeed falls to zero, the blade leading edge trajectory would no longer follow the rotor circumference but would transition to always lead the trailing edge in the aircraft flight direction. At the transition speed there is a bifurcation point in the blade orientation as it starts backward relative to the aircraft. In this mode the rotor rim speed relative to the aircraft is less than the forward airspeed. Lift and thrust available increase with aircraft speed due to increasing average blade airspeed. As critical mach for the blades is approached, the advancing blade angle of attack can be reduced to delay the formation of shock waves and wave drag.

The Challenge and Opportunity

The structural, inertial, aerodynamic, and control complexities inherent to the cyclogyro make construction of a working craft a significant challenge today. Nevertheless, advances in gas turbine engines, carbon composite structures, and control algorithms and processors for dynamic systems now make the cyclogyro possible and practical. Renewed patent activity in the last 15 years reflects this, although we are not aware of any serious attempts to construct a cyclogyro recently.

3 Phase I Technical Objectives

(The following is extracted from our phase 1 proposal.)

The technical objectives for Phase 1 are as follows:

1. Perform analysis of blade shapes, rotor solidity, and power requirements for a cyclogyro with a 6 foot total span and 2 foot diameter rotors. Use Wind-US or similar suitable CFD analysis software for detailed simulation o cyclogyro performance.
2. Perform structural analysis and design of the rotor blades.
3. Fabricate 8+ blades of approximately 3 inches chord, each 2.5 feet long. Design goals are light weight and high radially isotropic bending stiffness.
4. Design and fabricate blade support and control structures and assemble two rotors. The rotors will be used for static testing in Phase 1 and flight tests on a radio controlled aircraft early in Phase 2.
5. Static test the rotors with electric motors and torque measurement to measure static lift in and out of ground effect and to obtain appropriate blade angle settings for initial flight tests.

4 Phase I Work Plan

(The following is extracted from our phase 1 proposal.)

4.1 Task 1. Rotor Simulation

In this task we will simulate 2-dimensional flow through a cyclogyro rotor to predict blade interference effects and obtain blade angle related performance estimates across the range of possible aircraft speeds. This will validate and refine predictions from the 1930s and our initial work described below. If time permits, we may also perform some 3D flow analysis of hover, where 3D results are likely to differ most from 2D results. However, static tests will form the primary basis for hover performance analysis.

The CFD package is Overflow-D, a NASA-developed package for unsteady flow analysis and dynamic systems such as rotors and variable geometries.

4.1.1 Work to Date

We have performed a preliminary performance analysis using basic structural and aerodynamic principles. Our approach and the results to date are included here.

Simulation Conditions

A 4 blade rotor is modeled based on blade aerodynamics, an approach similar to that used for cyclogyro performance prediction in NACA TN-467 by Wheatley[1]. Each blade is 1 foot wide and 10 feet long. The form drag coefficient used is

$$C_{D0} = .015,$$

chosen as constant at an average value over moderate section C_l typical of symmetric airfoils such as NACA-0009 and -0012, although for high speed aircraft a symmetric supercritical airfoil[8] might be used.

The blade lift coefficient used is $C_L = .08\alpha$, where α is the varying blade angle of attack based on the instantaneous relative wind. Blade induced drag is taken to be

$$C_{Di} = C_L^2 / (\pi AR e).$$

We assume an Oswald efficiency of 0.8, and the aspect ratio of the blade is 10.

Other conditions are:

Rotor Speed:	50 rad/sec = 478 rpm
Rotor Diameter:	8 feet
Rotor Length:	10 feet
Blade width:	1 foot
Rotor Solidity:	0.159

Simulation Results

The resultant lift and drag from the momentary apparent wind velocity vector for any rotor speed, forward, speed, and angle of attack is then computed. These are resolved into radial and tangential forces for purposes of computing blade loads and power. They are also resolved into aircraft lift and thrust.

Hovering and Low Speed Flight

This underestimates induced drag at low speeds, where the aspect ratio should probably be that of the rotor as a whole and circulation must be taken into account. As with helicopters, cyclogyro hover power significantly exceeds the power required for forward flight as shown in Figure 1 and in the AH-64 Apache Power Required curves in Figure 5.

Therefore, for hover and low airspeeds we use the approach of Strandgren[9] who estimated cyclogyro power/lift from conventional propeller and helicopter theory. Predictions of cyclogyro hover performance use conventional static force momentum/energy balance. The hover analysis here treats thrust as vertical, while thrust in forward flight is in the flight direction.

With this approach we obtain a power/thrust estimate per rotor foot on our modeled rotor in two ways. The first is standard propeller theory.

The induced velocity V_i is [10]

$$V_i = 0.5 (-V_\infty + (V_\infty^2 + 2T/(\rho A))^{0.5}),$$

where V_∞ is the free stream (vehicle) airspeed, T is rotor thrust, and $A = 2RL$ where R is the rotor radius of four feet and L the rotor length. Then power in shaft horsepower is given by [10]

$$P = T (V_i + V_\infty)/(550\eta),$$

where thrust T is taken from a simulation of various α profiles through one revolution of the rotor. This is discussed below. Rotor efficiency η is assumed to be 0.8 though determination of this is one goal of phase 1 work.

With a thrust loading of 12 pounds/rotor foot using sinusoidal blade deflection with amplitude (and hence α_{max} since we neglect downwash and interference effects) of 12.4 degrees, this gives a static thrust (lift) / power estimate of 0.11 shaft horsepower / lb, or 106 shp for a rotor with 960 lb of static thrust. Induced velocity is 50 f/s. Recirculation in hover would likely result in an additional 50% power required. This agrees reasonably with NACA predictions and experimental results and modern helicopter maximum weight loadings in Table 1 [1][2][3][4].

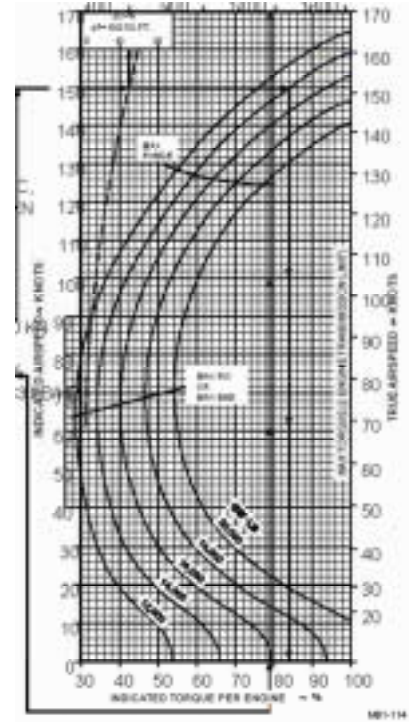


Figure 5. AH-64 Power Required vs. Airspeed for 5 Gross Weights

Vehicle	Weight/Load	Rotor Area	Disk	Disk/Rotor Loading	Lb / SHP @max weight
Robinson R22 Beta II	1370 lb	497 sf		2.75 lb/sf	.13 shp /lb
Bell 407	5500	963		5.71	.12 shp /lb
NACA Cyclogyro Prediction	1440	288		5.0	.10 lb/shp
NACA Cyclogyro test result	NA	64		5.0	.15 lb /shp
Acuity modeled	960	80		12.0	.11 to .16 lb/shp*

*It should be noted that the higher loading of the modeled rotor yields a number in line with the other, real-world values, reasonably suggesting that in hover, both for helicopters and cyclogyros, only about 50% of the theoretical lift is available. Also, the AGW values for the helicopters would necessarily include a safety margin.

Table 1. Representative Thrust Loadings and Power Required

Aerodynamic Modeling

The discussions below include results from our power estimates based solely on blade aerodynamics. The simulation proceeds from the computation of the lift and drag on each blade, treating it as a wing with aspect ratio 10 and Oswald efficiency 0.8. This is not expected to predict hover accurately, as the aspect ratio should probably be that of the rotor as a whole, and there is no allowance for recirculation. Accuracy should improve in forward flight.

Blade Loads in Hover

Blade lift in hover is sinusoidal, dropping to just below zero as the blades move vertically and reaching maxima during horizontal motion.

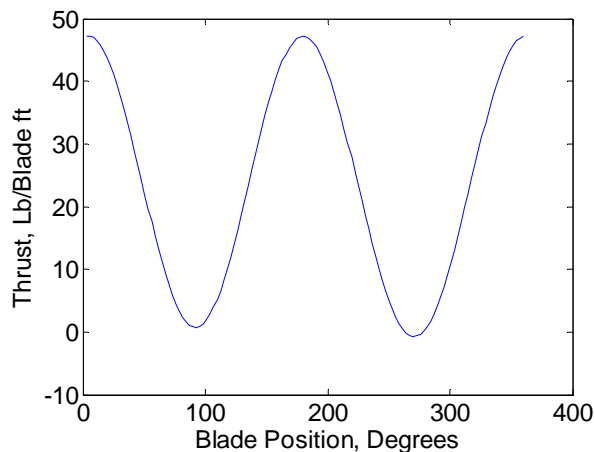


**Figure 6 .
Blade Thrust (Lift) in Hover**

Aerodynamic Compensation of Inertial Rotational Loads

The magnitude of the correction in C_l to yield balanced positive (outward) and negative radial force will depend on the blade mass, chord and rotor diameter, but not on rotor speed. If mass per foot is approximately proportional to chord (hollow blade of given skin thickness), the balancing requirement is also independent of chord, and there will be a minimum rotor diameter for a particular material at which correction is practical. If weight goes up with chord squared (hollow blade, but increasing skin

thickness with increasing chord), the minimum practical radius will increase linearly with chord, resulting in a constant attainable rotor solidity, which will also have an aerodynamic optimum point.

Assuming 0.8 lb/ft blade weight for a carefully designed 1 foot chord 12% airfoil of carbon composite and if we can afford C_L of .2, and with aerodynamic and inertial forces in equilibrium, we have

$$\text{Load per foot} = V^2/R \times \text{mass per foot} = q \times C_L \times \text{chord}, = .5 * \rho, \text{ so mass} = R \times .5 \times \rho \times C_L \times \text{chord}.$$

$$\text{mass} = .8/32.2 \text{ and so rearranging: } R = (.8/32.2) / (.5 \times .002378 \times .2 \times 1\text{ft}) = 104 \text{ ft}.$$

Thus it takes a 104 foot radius to allow effective aerodynamic cancellation of rotation loads in hover. With a radius of 10 feet, complete load balancing would require more lift than would be available.

We conclude that load cancellation in hover is not practical, and the rotor blades and control system must be designed to accommodate substantial loads and bending. Fortunately, the situation changes in high speed forward flight. Aerodynamic forces can be larger and more C_L is available as less is needed for propulsion.

We have not yet attempted to develop a blade angle function or power required curve for low speed forward flight (0 to 200 f/s). This will be part of the phase 1 effort. As speed increases from hover the phase of the blade tilt will be advanced to gradually vector thrust from vertical to the forward direction.

High Speed Flight

In high speed flight we wish to produce both lift and thrust. We also wish to minimize the radial load on the spinning blades. Finally, we wish to maximize the aircraft airspeed at which critical Mach is reached on the blades. The latter can be accomplished by maximizing blade lift when the blade is moving backward relative to the aircraft in its rotation, and reducing angle of attack to zero at the peak airspeed of the advancing blade. Since the blades are producing the aircraft lift, the aircraft need have no lifting wing reaching critical Mach, and the blade critical Mach will be the limiting factor in aircraft speed.

Taking these into account we have developed a function for blade angle relative to the aircraft at high speed. Model conditions are

Aircraft speed: 700 f/s,
Blade speed of 200 f/s,
Other conditions as in Sec. 4.1.1.1.

In phase 1 we will extend the analysis to include speed, desired thrust and lift variables.

Direction of Rotor Rotation

Blade rotation and incidence relative to the aircraft is shown in Figure 7. It is a sinusoid offset in phase and d.c. bias. Rotation is clockwise in Figure 7, which shows blade and relative wind angles. The rotation direction is chosen so that minimum blade airspeed occurs at the bottom of the cycle, where producing positive lift reduces centrifugal blade loads. High angles of attack can be used in this region without inducing critical mach on the blade. Blade angle of attack is very near zero at the top, at maximum blade airspeed, again to avoid shock formation. Angle of attack is shown in Figure 8.

If an aircraft is designed to operate near critical mach and blade bending is a limitation, the rotors will both need to rotate in the same direction. The dynamics of an aircraft with counter-rotating blades would

be quite different from those of one in which the rotors rotate together, since both pitch torque and gyroscopic forces would cancel rather than adding. This is a topic for further study in phases 1 and 2. See Stability and Control, below.

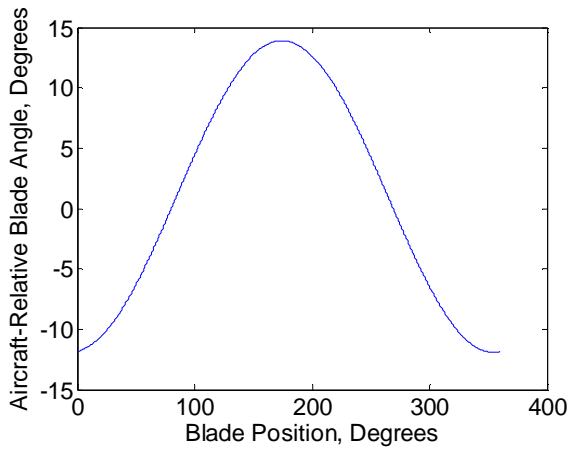


Figure 6. Blade Angle Relative to Flight Path

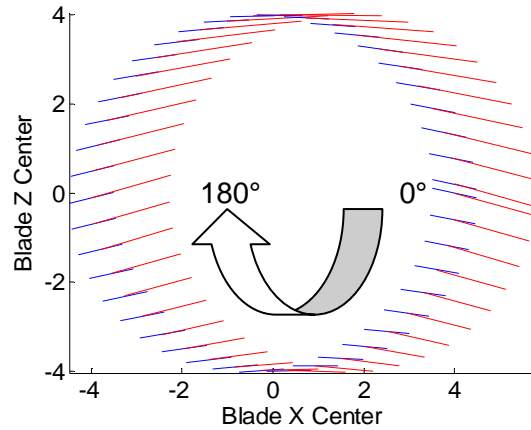


Figure 7. Blade Angle for Several Rotor Positions (Blue) and Relative Wind.

The aircraft thrust T in Figure 10 is obtained from the simulation of individual blade aerodynamics. θ is the angular position of the blade on the rotor. $\theta = 0$ when the blade is in the direction of forward flight from the rotor center. Horsepower per pound estimates are derived in two ways. The propeller theory result in Figure 14 is based on the rotor thrust loading obtained from the simulations. The blade based curve is obtained from resolution of blade aerodynamics into aircraft relative force components.

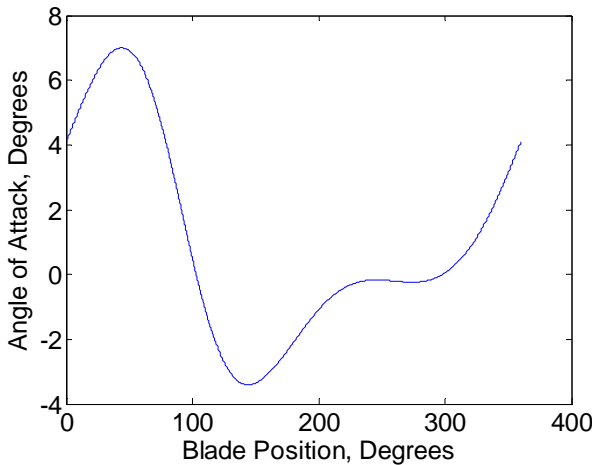


Figure 8. Blade Angle of Attack to Momentary Relative Wind (Zero at Maximum Blade Airspeed)

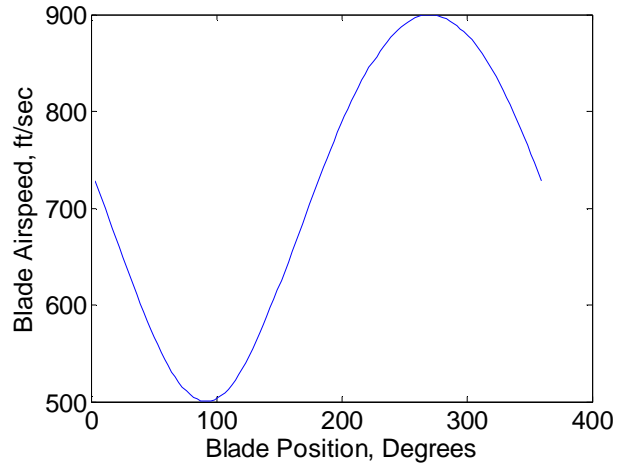


Figure 9. Blade Airspeed

It is worth noting that by adding a constant bias α_0 to the angle of attack normal to V_∞ , we are able to control the lift with only slight effect on the thrust and power. Also, thrust attainable increases with forward airspeed at constant angle of attack excursions. For this simulation the vertical blade bias α_0 was chosen to yield positive lift, which can be done without significantly affecting thrust or power. This is to be expected at high speeds, where induced drag is a small portion of total drag.

As forward airspeed increases, the NACA tests showed (Figure 3b) that power required decreases for speeds up to about 50 ft/s. At higher airspeeds, we expect that the blades can be treated individually with increasing accuracy.

The lift and drag forces on the blades are resolved into radial and tangential forces on the rotor and into aircraft thrust and lift forces contributed by a blade as it moves through 360 degrees in Figures 10-11.

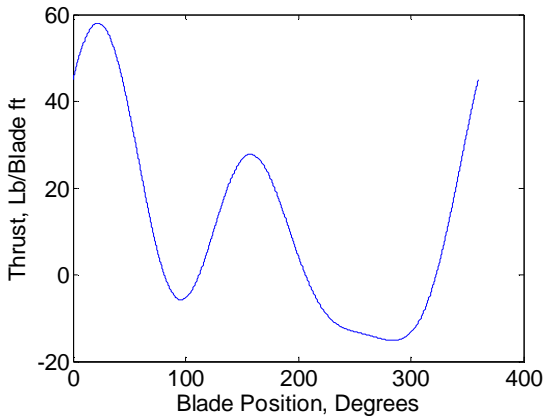


Figure 10 a.
Forward Thrust, One Blade

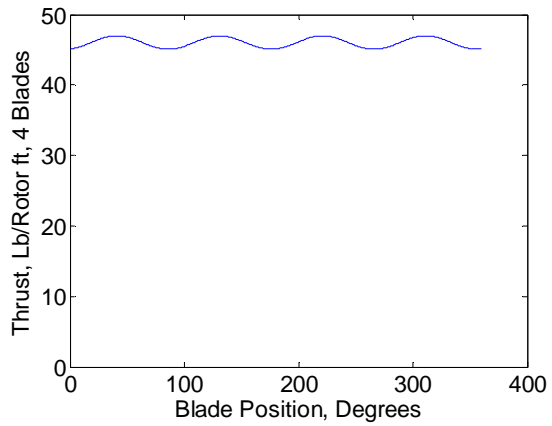


Figure 10b.
Aircraft Forward Thrust, 4 Blades

90° Apart.

Centrifugal force on a blade weighing 0.8 lb/ft is 248.4 lb/ft. Figure 12 shows blade aerodynamic radial forces and total radial forces including those due to rotation. The blade attitude has been chosen to reduce total radial forces. In phase 1 we will further investigate optimizing the blade angle as a function of blade position, although the function used here keeps total radial forces within 120% of inertial forces.

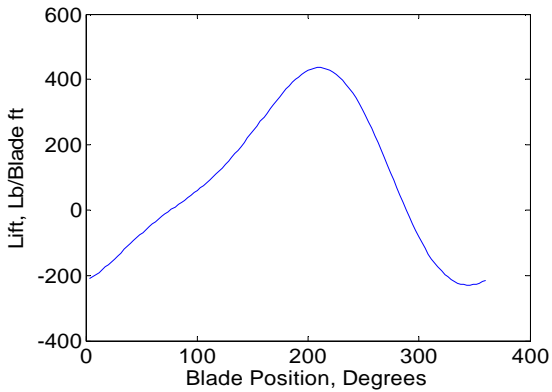


Figure 11a. Lift Forces From One Blade

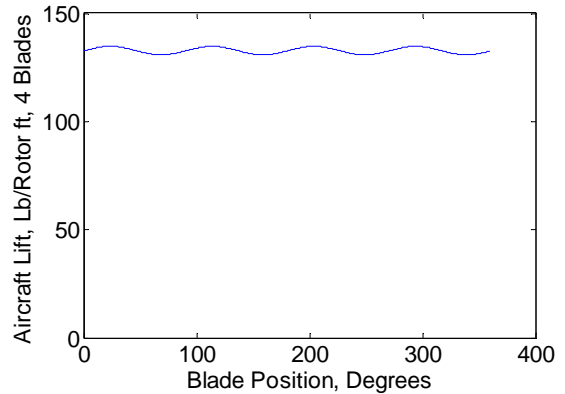


Figure 11b. Lift From 4 Blades

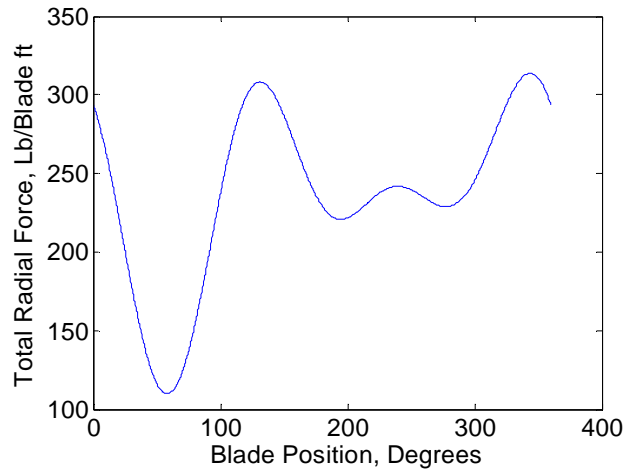


Figure 12. Total Radial Blade Force (Aerodynamic + Rotational)

Number of Blades and Force Fluctuation

The asymmetric nature of the lift and power forces shown above indicates that two blades will not eliminate force variations on the rotor support. However, the force variations are generally sinusoidal. With 4 blades the radial force fluctuations are on the order of 1% of the total radial forces, thus requiring little flywheel smoothing. Lift variations are less than 0.5 pounds per rotor foot. Thrust, acting in the direction of travel, has larger variations, approximately 2.5% of the thrust magnitude. A larger number of blades would reduce vibration, but aerodynamic blade interference effects would increase.

Figure 14 shows the estimates of power required from propeller theory and from our independent simulation of blade lift /drag. In both models $\eta=0.8$. We do not model compressibility: The increase in power above 600 f/s is due to the fact that the rotor is somewhat large for operation at these speeds. The difference at lower speeds is most likely due to our treatment of each blade individually, neglecting interference.

Lift Provided

An important contribution of the rotor in this simulation is the production of lift as well as thrust. Figure 13 above shows lift of 135 lb/rotor ft. at 700 f/s, 50% more than that assumed for hovering. This means that the power required to overcome the equivalent of wing drag has been included in the power consumption shown. Furthermore, rotors need not be designed and sized to fly at very low speeds. We consider the rotor size modeled here relatively lightly loaded for a high speed flight design. Finally, the rotor blade airspeed need not be higher than the aircraft speed when generating thrust and lift.

Although we have observed that power/thrust does not vary greatly for “reasonable” blade angle functions, optimizing the angle of attack function without critical mach avoidance will likely improve P/T, and the function will vary for varying airspeeds. In phase 1 we will investigate the optimization of blade angle for a full range of flight conditions.

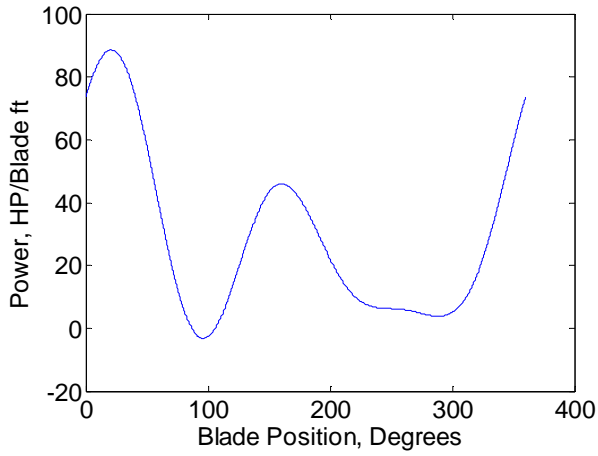


Figure 13a. Power for One Blade

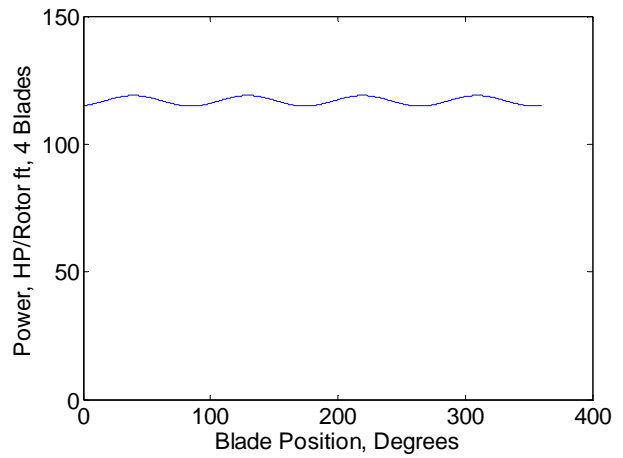


Figure 13b. Power for 4 Blades

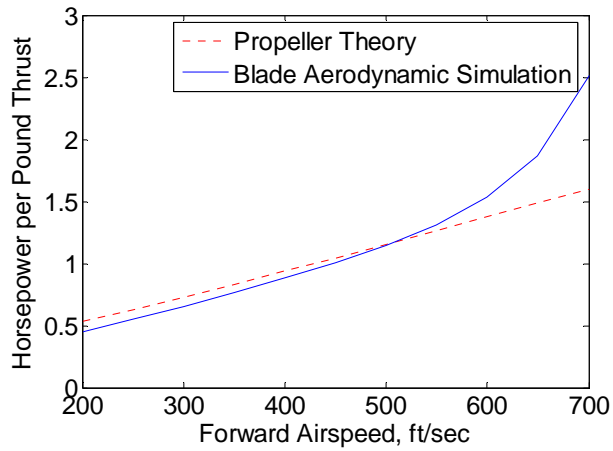


Figure 14. Horsepower per Pound Forward Thrust

Rotor Speed = 420 rpm, $\alpha_{max} = 6^\circ$ Across Entire Speed Range. Rotor Lift = 135 lb / rotor foot @ 700 f/s

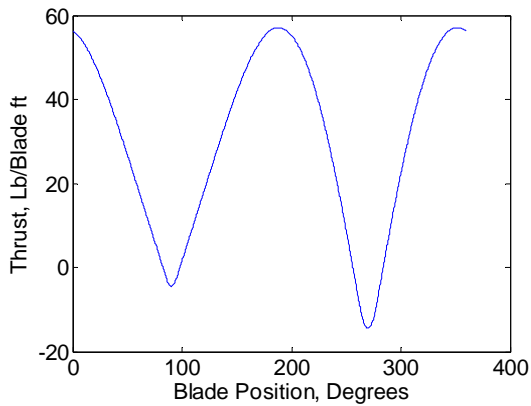


Figure 15. Thrust /Blade ft

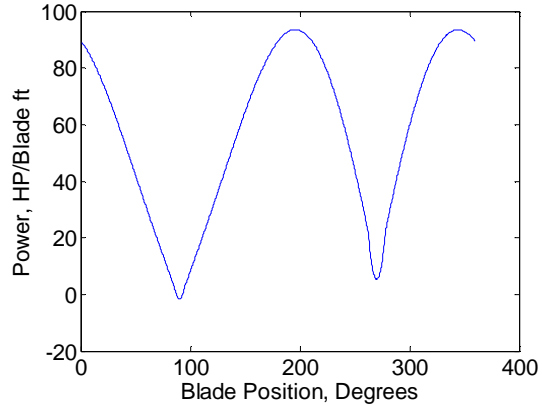


Figure 16. Power/Blade ft

Blade Angle Optimized for Maximum Thrust

Blade Angle Optimization

Figures 15 and 16 show the power and thrust results when blade angle is chosen to maximize thrust at each point in the blade rotation for $V_\infty = 700$ f/s, subject to $|\alpha| < 5$ degrees. This is not necessarily a global optimum, as it may be advantageous to forego thrust generation entirely at some points in the cycle where attainable P/T is below the average attainable. It also leads to many unrealizable conditions at 700 ft/sec, but the resultant power/thrust is 1.88 hp/lb, very close to the value of 1.68 from propeller theory. This is also a useful way to obtain what desirable blade angle function approximations.

A multivariate nonlinear optimization will be developed in Phase I. using constraints on blade angle rate, CL and CL/CD, thrust vs lift, maximum blade force and other variables. Blade angle functions for hover, best power, best cruise range and loiter can be developed. Matlab's optimization functions make solution of such problems straightforward once the formulation has been decided upon.

Rotor Solidity

The cyclogyro rotor solidity σ is defined as [2] $\sigma = bc/2\pi R$, where b is the number of blades.

NACA's work concluded that an optimum solidity was about 0.1. For small chords (low solidity), we have used the simplification that the curved path of the blade through the air can be treated as momentarily straight. As chord increases, this assumption and the question of adding camber to the airfoil will become significant, although in high speed flight the blade path through the air is not sharply curved. In phase 1 our test rotors will use symmetric airfoils, and we will analyze the behavior of straight and curved airfoils with US-Wind.

4.2 Task 2. Blade Weight, Loads and Bending

The blade model used in our bending and weight analysis is shown in Figure 16. It has a carbon center spar/skin section, and fiberglass or other material for leading and trailing sections. The weight of the carbon/epoxy construction is 0.207 lb/ft. For a blade with a 12 inch chord, and 1.2 inch thickness the skin and shear web have a total cross sectional area of 0.621 sq in, and the carbon portion of that is up to 0.086" thick with an area of 0.242 sq in. The fiberglass is 0.025 inches thick with a total cross-sectional area of 0.379 sq in.

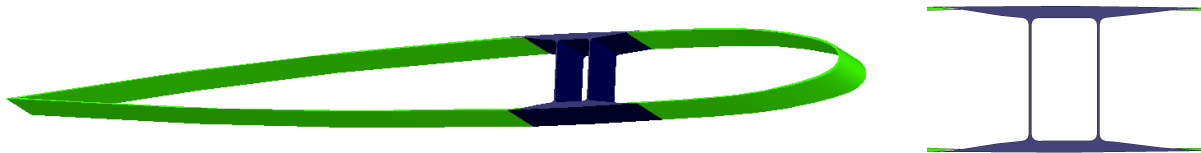


Figure 16. Two-Material Blade with Radially Isotropic Bending Stiffness

Deflection of the rotor blades must be possible while the blades are bent due to the forces on them. One way to promote this is to design the blades with uniform stiffness in all radial directions from the support axis. This will be accomplished by varying the skin thickness and the structural material around the airfoil section. Low modulus material will be used at the leading and trailing edges, and high modulus carbon in the center section.

Beam stiffness increases with the square of the beam dimension. To give the wing uniform bending stiffness in every direction from the support axis near the center of pressure a material with a low modulus, about 1% that of carbon, is required for the leading and trailing edge regions. Kevlar has about half the modulus of carbon. Fiberglass is impact resistant, but still of 20 to 30% the stiffness of high

modulus carbon even when chopped glass particles are used. Tensile strength and modulus for some typical unidirectional fibers appear in Table 2 [11][12].

Property	E-glass	Carbon	Aramid (Kevlar 49)
Tensile strength, MPa	2400	3100	3600
Elasticity modulus, GPa	70	220	120
Elongation to break, %	3.5	1.40	2.5
Density, g/cm ³	2.54	1.75	1.48

Table 2. Fiber Properties

Property	Polyester	Epoxy
Tensile strength, MPa	40-90	55-130
Elasticity modulus, GPa	2.0-4.4	2.8-4.2
Impact strength of notch, J/m	10-21	5-53
Density, g/cm ³	1.10-1.46	1.2-1.3

Table 3. Matrix Properties

For non-spar portion of the blade, fiberglass is denser than carbon at 2.54 gm/cm³, or 2.54 × 62.4 lb/ft³ = 158.5 lb/ft³, so the fiberglass weight is 0.417 lb/ft. Total blade weight is then 0.783 lb/ft.

Un-reinforced matrix properties are shown in Table 3. These matrices have a low modulus, 1% of that of carbon fiber/epoxy. If combined with a low modulus, high strength plastic fiber, the density is half that of fiberglass and a thicker wall can be used.

The mass and EI (modulus × area moment of inertia) of the blades determine the bending stiffness[13]:

$$\text{Sag at center} = W \times (L^3) \times 5/(384 \times E \times I) ,$$

where L is the beam length, E = Young’s modulus, I = area moment of inertia, and W is the total uniformly distributed force on the beam.

For a blade of airfoil thickness 2a with a spar consisting of two caps of thickness h and width b[14]:

$$I = 2 \times (b \times h^3/12 + a^2 \times b \times h).$$

The load on the blade due to rotation and the blade weight is

$$W = \omega^2 R \times \rho \times b \times h \times L,$$

where ρ is the density in slugs/ ft³, and L is the length of the blade.

Assuming the carbon center section provides all the stiffness and the division of cross-sectional areas and material densities for fiberglass and carbon-epoxy, bending of 0.37 feet over a 10 foot unsupported span of 10 feet will occur in a 10 foot blade simply supported on both ends. This is slightly conservative as it does not include the slight additional stiffness of the skin other than the carbon structure, but does include the additional weight.

Elongation to break can be calculated from tensile strength / modulus and is 2% for these resins. Since the blade will be designed for isotropic stiffness, the amount of bend for a given load will be independent

of the blade orientation. Figure 17 shows a blade bending in the plane of the chord line (leading or trailing edge at maximal inner or outer radial position). The calculated bend of 0.368 feet radially is approximated as a circular arc. The inner arc length is 9.76' and the outer arc length 10.05'. This is a 3% difference between maximum compression and maximum elongation. Most of the extension and compression will occur at the trailing edge, the point most distant from the carbon spar structure. The actual amount would depend on the amount of extension of the spar, but maximum extension at the trailing edge could exceed 3%. so a material with greater elongation/compression should be used. Additionally there should be a structural element stiff in the direction from top to bottom of the airfoil near the leading and trailing edges to prevent bending out of the radial plane in compression, which would affect the blade angle of attack.

The above are first order calculations to check the feasibility of constructing useful blades. Design of full scale rotor blades will be done with CAD tools for computing stiffness in any axis to obtain blades of uniform stiffness.

For the blade to be easily controlled, the support should be located at the center of pressure. Since the center of pressure moves with angle of attack, the height of the support/pivot axis (position along axis normal to chord line), if one axis is used for both, should be chosen such that the center of pressure passes through it, or nearly so, over the operating angle of attack range. Using the aerodynamic center as the support point could make it difficult to compensate the pitching moment with the pitch actuator, since a non-zero C_m , constant or otherwise, will result in a varying torque across operating conditions.

Blade Stresses

The desire to minimize bending to ease pitch control has driven our wing construction model. Spar stresses have not been calculated explicitly. However, since the bending corresponds to a 3% elongation over a one foot change in radius, a spar of 0.6 inches half height would be expected to extend/compress only about 0.15%, so we expect the loads will be only about 10% of the breaking strength of the spar. The blades would be designed to take maximum C_L at V_{ne} . Note that none of these calculations include safety factors, which would be reflected in a lower maximum rotor speed, about 30% for a 2x safety factor. Safeties should also be built into any rotor design to feather a blade if maximum bending loads are exceeded.

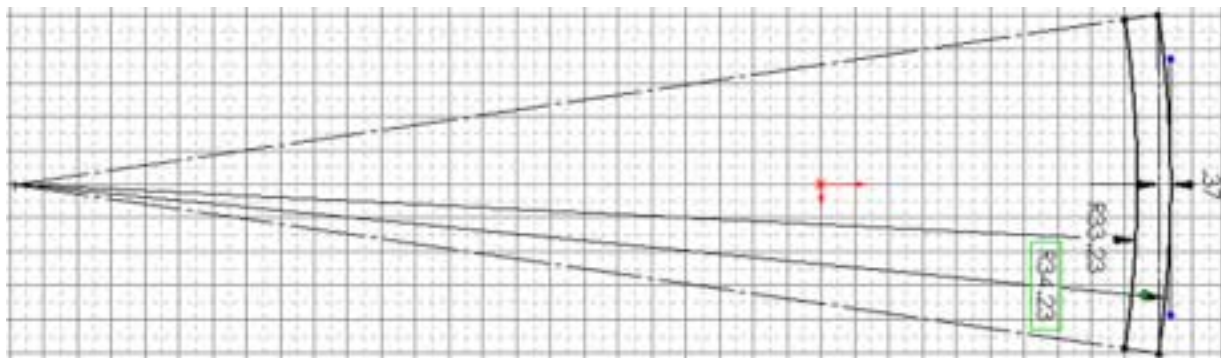


Figure 17. Blade Bending and Elongation at Radial Incidence

4.3 Task 3: Phase 1 Rotor Blade Construction

The first test rotors will be designed and built with materials suitable for a flying aircraft. This will maximize the experience with the materials and



processes to be used in phase II. If the rotors work well enough they will be incorporated in the first phase II flying aircraft.

The phase 1 blades will be small, about 3 inches in chord with 0.3 inch thickness. They will be made with commercially available hollow carbon tube for the main spar, and high density foam for the airfoil shape, similar to the airfoil at right. The stiffness of the foam is low enough that the airfoil stiffness will be very nearly isotropic. The foam may have additional hollows in it to place the center of mass at the center of the spar. The blades will then be covered with a flexible Mylar model aircraft covering.

The airfoils will be cut by a foam cutting house such as FlyingFoam[15] or Compu-FoamCore [16]. Appropriate tubing is available from CST Sales[17]. A suitable foam is Airex[18] C70 High Stiffness Foam, 3.85 lb/cu ft.

The amount of bending in a beam supported at both ends increases with the cube of the length. For a given blade airspeed, it also increases with the inverse of the rotor radius. The phase 1 rotors will be $\frac{1}{4}$ the size of the rotors Acuity has modeled: 2.5 feet long with a 1 foot radius. Expected bending is still only $\frac{1}{8}$ to $\frac{1}{16}$ that of the full size blade, or about $\frac{1}{2}$ inch at the center at an airspeed of 200 f/s at about 1900 rpm. These are similar to model helicopter blade speeds and dimensions, which reach over 2000 rpm with 400 ft/s tip speeds.

4.4 Task 4: Rotor Design and Fabrication

4.4.1 Blade Control Concepts

The actuators for the blades will be driven by a control system that uses current blade positions, attitudes, the current forces on and state of the aircraft, and command inputs. A 6 DOF inertial sensor in the aircraft will provide acceleration and angular rate inputs. This information will be combined with airspeed and the blade angle to force functions, as well as the dynamic model of the aircraft-rotor system to generate control outputs.

There are two approaches to blade control. One is the individual active control of each blade. This would allow the most general form of control, including rapid pitch changes to optimize rotor performance based on considerations such as the best angle of attack profile when passing through the wake of other blades. However, it is also relatively difficult to implement.

Another approach is to use only combinations of sinusoidal motion. Either individually or all together, the four blades can be driven by a mechanism that does not require actuator motion except when the rotor behavior must be changed. This allows actuators to make smaller, slower movements rather than active changing the pitch of each blade as a function of position. For performance testing of a specific condition, no powered actuators are needed. The eccentricities that control blade pitch variations can be set and locked in.

In early Phase 1 CFD work it became evident the sinusoidal incidence angle profile that could be attained with the type of mechanical drive system described in our proposal would not be adequate to obtain reasonable performance, so programmable motors slaved to the main drive motor encoder were built into the blades and a servo control system added that rode on the spinning rotor, along with batteries and a wireless data acquisition system. The additional complexity resulted in the construction of only one rotor rather than two, but was more significant to proof of concept.

4.4.2 Task 5: Static Testing

Static tests will be carried out to measure the lift that is produced by a the model rotor system. This will be conducted both near a ground surface and at least two rotor lengths from a surface, to measure the magnitude of ground effect on lift amplitude and direction. A 2 HP electric motor will be used to supply power and the rotor speed will be measured with an attached encoder or optically or acoustically. A torque measuring coupling will be installed between the motor and the rotor so that power may be directly computed. The parameters to be varied include rotor speed and blade shift in the three degrees of freedom provided by the pitch controller.

4.5 Phase I Schedule

Phase I Hours						Total	Name	Task	Description
Month	1	2	3	4	5				
	1	2	3	4	5	6			
	2	2	2	2	2		10	Clark	1010 Technical Oversight
		2	2	2	2	2	10	Clark	1020 Administrative Oversight
			20	20			40	Clark	2010 Aerodynamic Analysis
20	40	20					80	Clark	2020 Rotor Design and Analysis
	30	20					50	Katsouras	3000 Component Identification
									Mech. Assembly and
				40	40		80	Katsouras	4010 Integration
					20		20	Clark	6010 Rotor Test
					20		20	Katsouras	6010 Rotor Test
					20	20	40	Clark	7010 Control System Design
						20	20	Clark	7020 Results Analysis, Reports
							370		

5 Potential Applications

5.1 Potential NASA Commercial Applications

A practical cyclogyro would provide a NASA with a versatile, capable observation platform, chase plane, and instructional aeronautics demonstrator, as well as a test vehicle for improving cyclogyro flight characteristics and efficiency.

5.2 Potential Non-NASA Commercial Applications

The benefits of a VTOL capable craft that can approach the speed of sound in forward flight without radical reconfiguration are many, including convenient commercial transportation, rapid disaster/rescue response, and flexible multi-mission defense vehicles. We propose that the realization of a successful cyclogyro design can be accomplished with revolutionary structural and aerodynamic innovations, and a successful cyclogyro would be a revolutionary subsonic aircraft.

6 Contacts

6.1 Key Contractor Participants

- **Bob Clark – Principal Investigator**
 - Rotor aerodynamics, design, and control system.
bob@acuitytx.com

- **CJ Taylor – Staff Scientist**
 - Rotor CFD simulations, Wireless rotor communication
cjtaylor@acuitytx.com

- **Kevin Ciocia – Mechanical Engineer**
 - Construction of the rotor and drive system.
kevin@acuitytx.com

- **Ted Katsouras – Senior Technician**
 - Wiring, electronic assembly
ted@acuitytx.com

6.2 Key NASA Participants

Technical Liaison
Richard Maine
661-276-3316
Richard.Maine@nasa.gov

6.3 NASA and Non-NASA Advisors

None.

7 Technical Activities

7.1 Cumulative Technical Activities

7.1.1 Phase I Technical Accomplishments

In phase 1 we have shown that cycloidal propulsion with real-time individual blade angle adjustment is a practical form of lift and thrust for subsonic aircraft. The technical accomplishments in Phase 1 are as follows:

1. Designed a cyclogyro rotor for construction and testing. This step consisted of airfoil design, blade structural design and calculations, main drive motor and blade motor and servomotor controller selection, incorporation of wireless equipment in the rotor to transmit data from the rotating frame to a workstation, and design of a battery power system for rotor electronics and drive motors.
2. Performed CFD analysis of blade shapes, rotor geometry, and power requirements for a cyclogyro with a 6 foot total span and 2 foot diameter rotors. NASA's Overflow-D CFD code capable on unsteady flow analysis, was used to evaluate rotor and blade torque and power requirements. Analyses were performed for hover and for high speed forward flight.
3. Fabricated 4 blades of 2.56 inch chord, each 2.5 feet long. The blades are light weight and have high radially isotropic bending stiffness. Blade angle drive motors are mounted in the center of each blade.

4. Designed and fabricated blade support control, and drive systems and assembled one rotor. The rotor was used for static testing in Phase 1 and will be used flight tests on a radio controlled concept demonstration aircraft early in Phase 2.
5. Performed static tests the rotors with electric motors and torque measurement to measure static lift in and out of ground effect and to obtain appropriate blade angle settings for initial flight tests.

7.1.2 Design Changes

Three significant changes to the initially proposed design were made:

1. The addition of a central rotor spar to transmit motor torque from the end of the rotor to the center.
2. The use of torque motors on each blade for controlling blade attitude relative to the rotor arm. In early CFD runs it became evident the sinusoidal incidence angle profile that could be attained with the type of mechanical drive system described in our proposal would not be adequate to obtained reasonable performance, so programmable motors slaved to the main drive motor encoder were built in and a servo control system added that rode on the spinning rotor, along with batteries and a wireless data acquisition system. The additional complexity resulted in the construction of only one rotor rather than two, but was more significant to proof of concept.
3. Load cell tension sensors were added to the rotor tension struts to allow direct measurement of forces on the blades after CFD runs showed relatively large, high rate force fluctuations during rotation.

7.1.3 Blade Airfoil Design

A modified Bell AH-1 Airfoil (in turn a modified NACA 0012) was thickened to 13.5% and cambered with the circular rotor path. This airfoil was chosen for its relatively high maximum lift and low pitching moment variation, as shown in Figure 1. The thicker chord is used for additional stiffness, as up to 13.5% it was found to have minimal effect on the lift and drag characteristics.

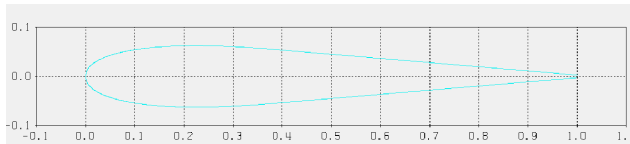


Figure 1a. Bell AH-1 airfoil thickened to 13.5%

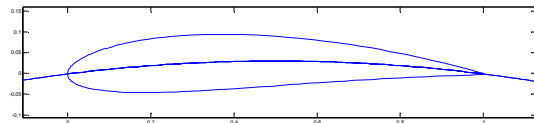


Figure 1b. Cambered with the rotor tip path.

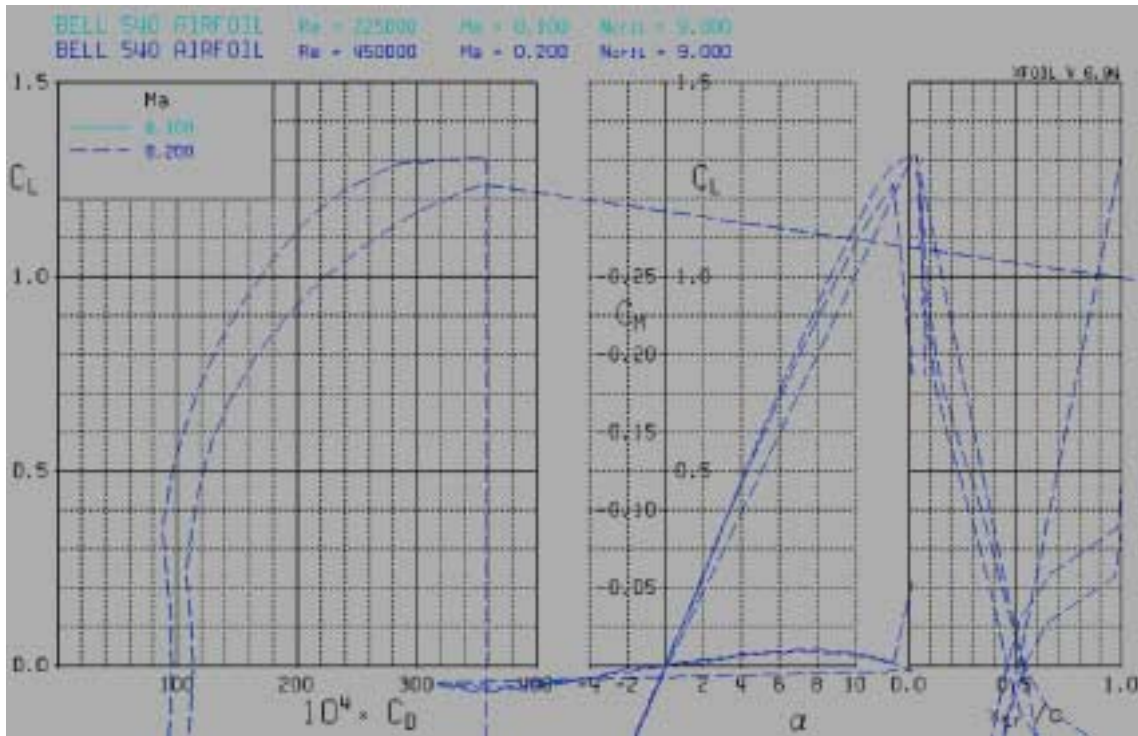


Figure 2. Airfoil Characteristics from Xfoil at Re = 225,000 and 450,000 (100 and 200 fps)
Moment at .23c

7.1.4 CFD Work

Acuity has performed a number of 2D CFD simulations of the rotor in operation using NASA's Overflow-D code on a Linux workstation. Overflow-D can simulate viscous non-steady flow and so was appropriate for this analysis. Each simulation was run at 1 degree steps for 10 rotations of the rotor. Steady state was generally established in 5 to 7 rotations.

The goals of the runs were to predict the forces and torques that can be expected on the blades and drive spar fairing and to identify a preliminary blade incidence angle profile that produces uniform, low vibration rotor lift and thrust in hover. Free stream velocity above and below the rotor is initialized to zero, but increases as the rotor turns. This results in gradual loss of lift over the course of the simulation. The actual steady state hover performance, as with helicopters, will be affected by the amount of circulation that develops.

Initial classical aerodynamic analysis indicated that a sinusoidal blade incidence angle relative to the rotor drive arm would be a reasonable starting point. The results from initial CFD runs were less than ideal so various modifications to the profile were tried. Our current profile along with the sinusoidal profile is shown in Figure 3. This profile pulls air from the upper semicircle around the rotor and propels in downward, much like a propeller in static thrusting conditions. This can be seen in Figure 7, which shows the high speed jet exiting below the rotor. Maximum velocity in the jet is approximately 0.5 times the blade speed.

7.1.4.1 An Overview of Overflow 2

7.1.4.1.1 Structured Grids, Boundary Conditions and X-ray cutting

As a first step to understanding the Cyclogyro Rotor, we undertook a series of Computational Fluid Dynamics (CFD) simulation runs using the Overflow 2.0 package. We developed grids for a 2D model of our rotor using Chimera Grid Tools (CGT). Both of these packages are freely available to U.S. companies from NASA Ames and Langley.

Each volumetric grid has an internal coordinate system with i, j and k axes describing the edges of the grid volume, thus every grid cell can be specified by three indicies. The critical difference between these axes and a 3D Cartesian grid is that the axes directions can vary for every cell. Using CGT, the structured grids axes directions can be made to vary in a smooth and continuous fashion which also accomplishing volumetric coverage. Each specified volume has an integer i_{max} , j_{max} , and k_{max} value yielding a total number of cells equal to $(i_{max})(j_{max})(k_{max})$.

The four blades shown in the figure to the right is composed of a single structured grid. Each blade volume is similar to a cylindrical coordinate system; one axes (l) is perpendicular to the page, one axes corresponds roughly to a “theta” axes circling the blade (j) and the last axes (k) denotes the radial distance from the surface of the blade. We engineered the grid density to be deliberately denser closer to the blade and at the blade head and tail. This allows Overflow better convergence as the vector and scalar fields are changing most dramatically in these regions.

Using Overflow, each grid can specify a variety of custom parameters about the flow conditions in that grid, but perhaps the most important are the boundary conditions (BCs), if any, for the border grid cells at beginning and end of the axes. Each BC in Overflow has a unique number associated with it. For our four blades, three unique BCs are employed. The inner radii (corresponding the surface of the wing itself) is specified as a Viscous adiabatic wall (5). The “theta” axes has a periodic BC (10) set to tell the solver that this particular axes wraps around on itself. The last axes (into the page) is specified to a special BC (21) which tells the solver that the problem is 2D in nature.

Overflow grids should naturally fall on top of one another to ensure overlapping coverage. The orange Cartesian grid in the preceding figure overlaps with all four blades volumes (it is additionally overlapped by six adjacent Cartesian grids (not shown)). Small overlapping regions between structured grids is encouraged for proper Overflow field solving, however large overlapping regions (such as the blades and the dense Cartesian grid) are a waste a CPU resources as typically only one grid (in this case, the high resolution and optimally oriented blade grids) is appropriate for solution finding.

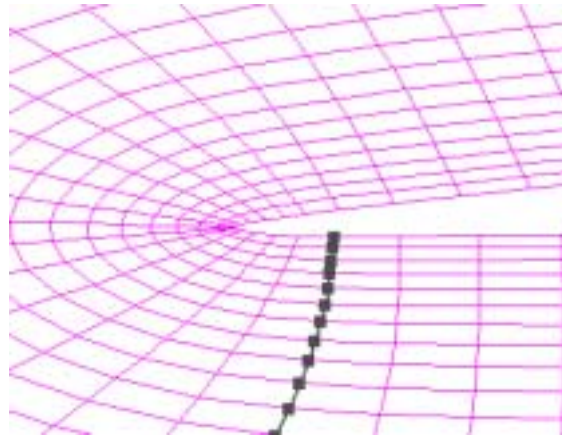


Figure 3. Closeup of the tail of one of the blades. The gray points show a line with a constant j-index

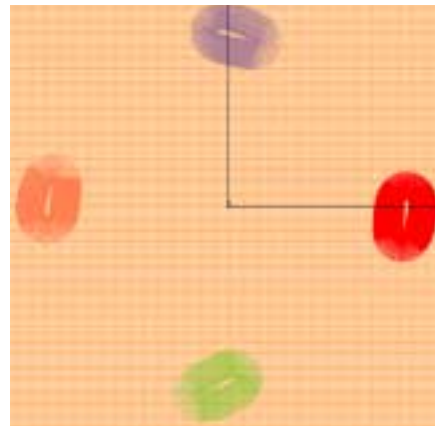


Figure 4. Four structured overset grids surrounding each of the four Rotor blades at their initial positions. Our blades are numbered 1,2,3 and 4 for the 3, 6, 9 and 12 o'clock positions respectively.

To eliminate much of the overlap redundancy, Overflow employs an X-ray cutting technique so named because it is akin to sending a beam of coherent X-rays through the original 2D surface - the Blade itself – which gave rise to the 3D grid. By noting where the X-rays entered and exited the object, a sparse outline of the 2D surface can be created. This Outline / X-ray file is efficiently used by Overflow to remove overlapping grid cells within a certain distance of the surface. Efficiency in computation is essential as in a problem with moving grids, the grid overlapping regions will have to be calculated for every iteration cycle.

7.1.4.1.2 Moving Grids in Overflow

Overflow allows complicated grid motions to be specified in a highly readable XML file. Individual grids can be transformed to their starting coordinate by using a Config.xml file. A complimentary Scenario.xml file describes the motion (if any) for each of the grids in terms of one or more body or inertial specified translations and/or rotations. The desired velocities can be expressed as analytical functions of t (time) of complexity up to the Fortran parsing buffer (hard limited at approximately 255 characters).

Our desired blade motion is fairly complicated, however it is periodic with respect to the main rotor period. To express it as an analytical function, we fit the first 9 terms of a Fourier Transform to the function (using more terms produces a Fortran parsing error), yielding a curve matching our desired profile to a high degree of accuracy. Our Matlab script takes a desired blade profile and automatically generates the necessary Config.xml and Scenario.xml files. In this way, we can rapidly update and run a new simulation after each perturbation to the wing profile.

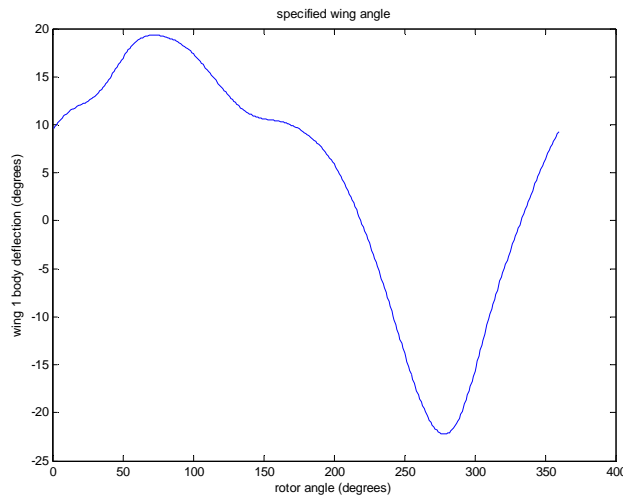


Figure 5. Specified Angle for Wing 1 as a function of the main rotor angular position

7.1.4.2 CFD Results

7.1.4.2.1 CFD Setup and Parameters

Here are some specifics for the 2D CFD simulation of the 4 Wing Cyclogyro rotor Configuration: The rotor is set to spin at 200 radians/second. The blades are 2.54” in length and rotate in a 12” radius circle. Together with the rotation rate, this corresponds to a reference mach number of 0.1845. Automatic far field grids were not used; the far field grids were manually added to the simulation. Each run used 3600 iterations with 1 degree of rotation per iteration. The Reynolds Number for the blades was 266,400. Overflow Boundary Condition (BC) 37 was used on the borders of the far field grids to ensure egress for the generated flow. As previously mentioned, periodic BC 10 was used to close each blade, BC 5 (Viscous adiabatic wall (pressure extrapolation)) was used for the surface of each blade. All grids had BC 21 (2D simulation) specified for their Y-axis BC.

7.1.4.2.2 Graphical Summary

The rotor reference frame and rotation direction are shown in Figure 6. Our blade angle profile went through a number of iterations before we settled on the final blade profile. The most significant observation is that there is a 5 degree asymmetry between the top (12 o'clock) position and the bottom (6 o'clock) position. The extra deflection at the 6 o'clock position is necessary to maintain angle of attack in the presence of the jet airflow. The jet is best visualized by the sequence of frames shown in Figure 7 below:

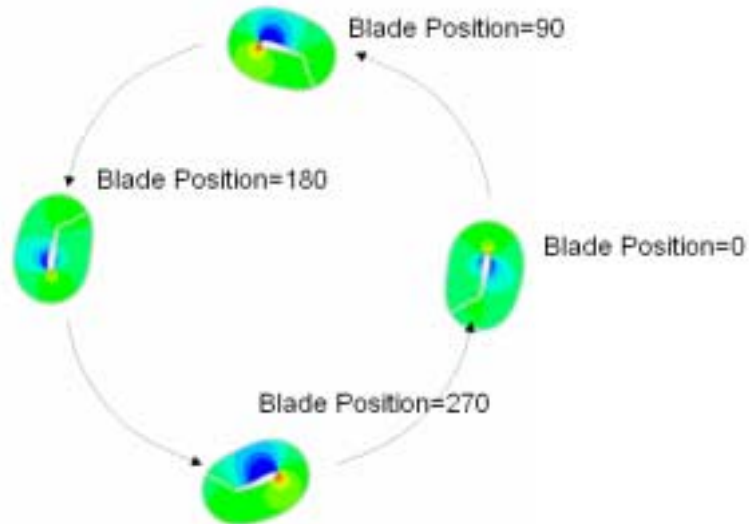


Figure 6. Rotor orientation reference

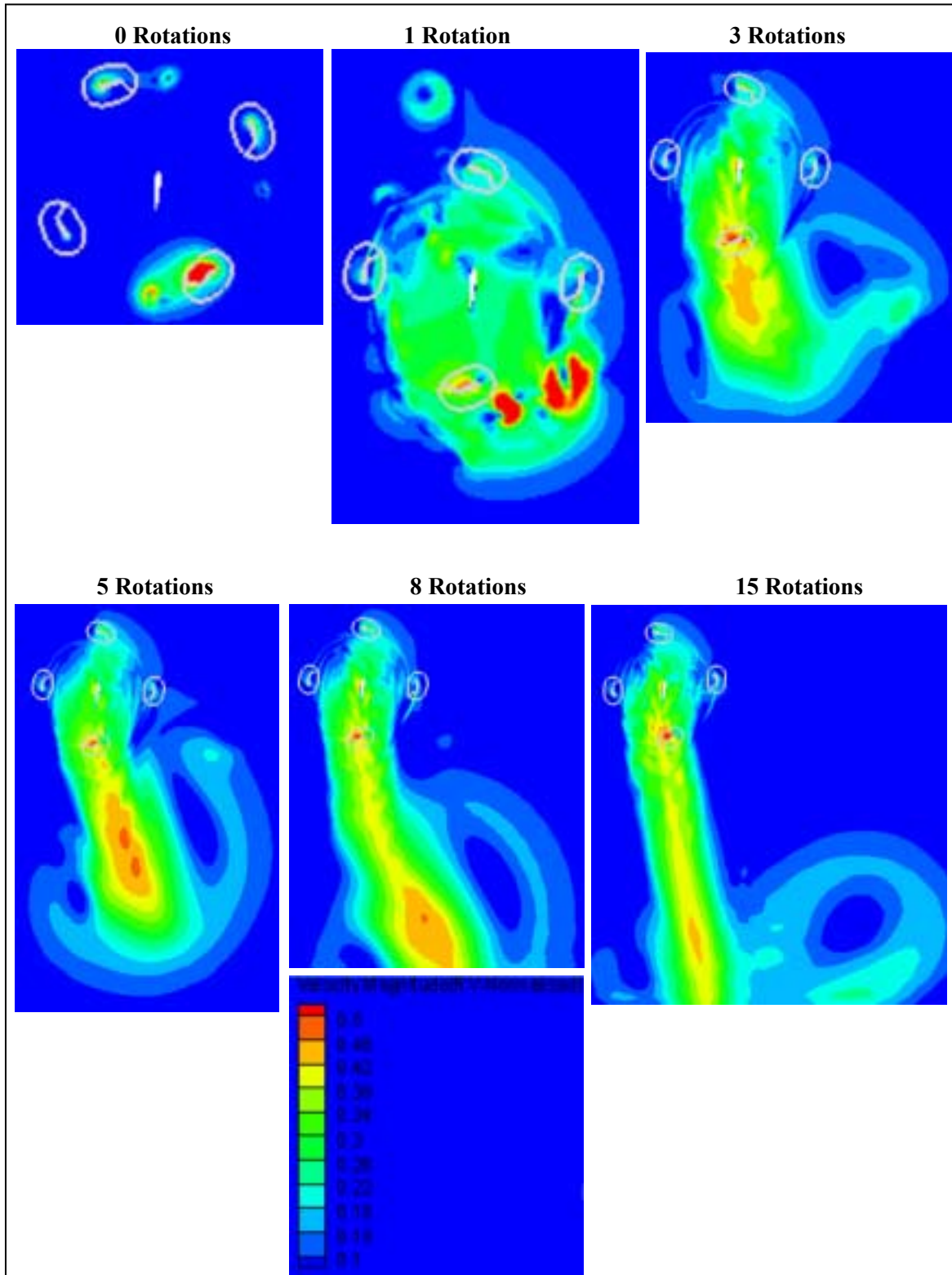


Figure 7. Rotor startup and jet snapshots. Airflow velocity is shown as a percentage of rotor speed. The rotor was rotating at 200 rads/second and with our 12” radius, this implies a reference mach of 0.184. The maximum air speeds observed in the jet are about 50% of that figure.

As the blade enters the jet, the motion of the air becomes almost as significant to the observed airflow by the blade as the motion of the blade itself (up to 50% as significant). Because of this, the blade needs to turn into the jet more to maintain lift and to prevent stalling. While this conclusion might seem obvious in retrospect, it wasn't immediately obvious to us when we designed our first blade profile.

One technique that we found useful in visualizing the blade forces working was to generate pressure movies of a tracked single blade throughout the 360 rotation. The figure below shows 8 frames spaced approximately 45 degrees along rotation of the rotor. In the blade's reference frame, the stagnation point alternates between being on the bottom of the blade (when the blade is right side up around the 12 o'clock position) and being on the top of the blade (when the blade is inverted at the 6 o'clock position).

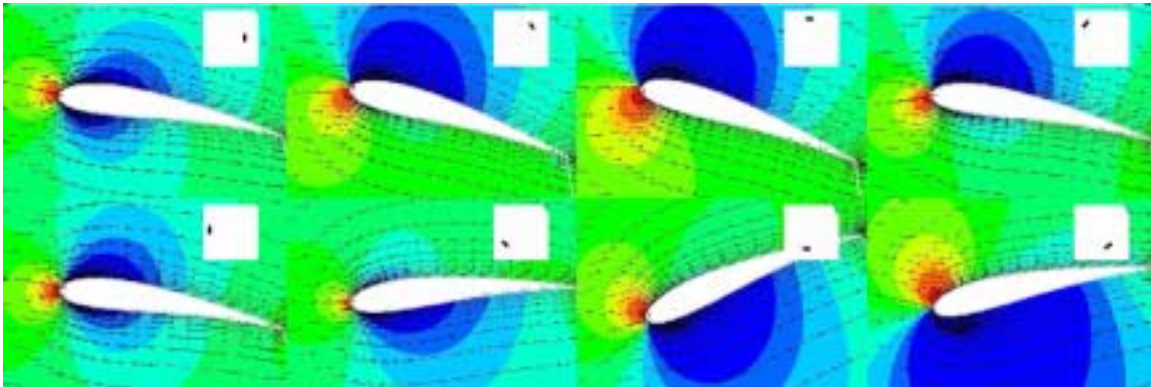


Figure 8. Velocity flow (black lines) and pressure scalar fields (blue = low pressure, red = high pressure) on a single blade as a function of main rotor position. The position of the blade is indicated by the black iconic insert. Note how the net force on the blade is greatest in the right six frames and minimum at the 3 and 9 o'clock blade positions (left two images). This corresponds to the desired goal of producing a large vertical force. The relative direction of airflow in the 3rd frame from the left in the bottom row is distinctly different from the other 7 images. This frame is taken from the center of the jet. The blade angle for this frame is deflected the most to maintain the blade's angle of attack.

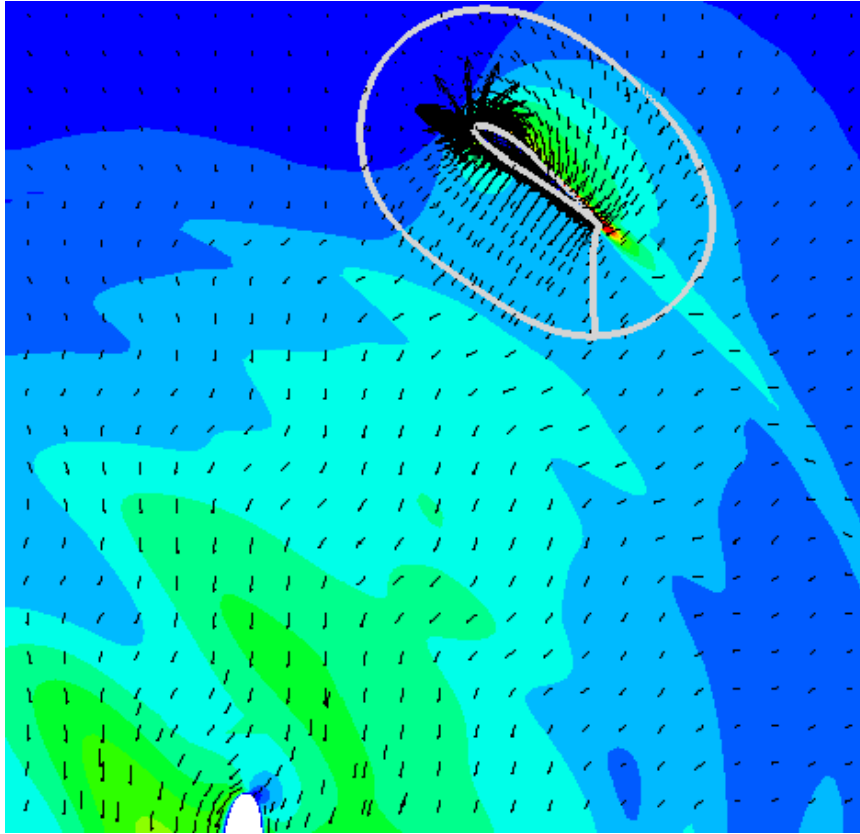


Figure 9. Velocity arrows showing fluctuations in air stream direction caused by passing blades. Note how there are kinks in the flow lines in the top right (1 o'clock) of the rotor core corresponding to the periodic passing of each blade. Additionally, there are localized pockets of higher (yellow/orange) and lower (blue) pressure within the jet itself. Compensating for these high frequency effects is extremely challenging. The center weathervane was a later addition to our simulation, but had little effect on forces.

The jet necessitates adding additional deflection as the blade enters the jet to maintain an appropriate angle of attack. Additionally, the jet contains higher frequency phenomenon; e.g. kinks in the vector flow field resulting from the periodic passes of the blades and localized regions of lower or higher pressure respectively as seen in figure below. It is an extremely challenging problem to compensate for these high frequency effects with realistic (i.e. power -constrained) wing profile. As we will see from the force profiles in the next section, we found it difficult to compensate for frequencies higher than the 7th or 8th harmonic of the rotor speed.

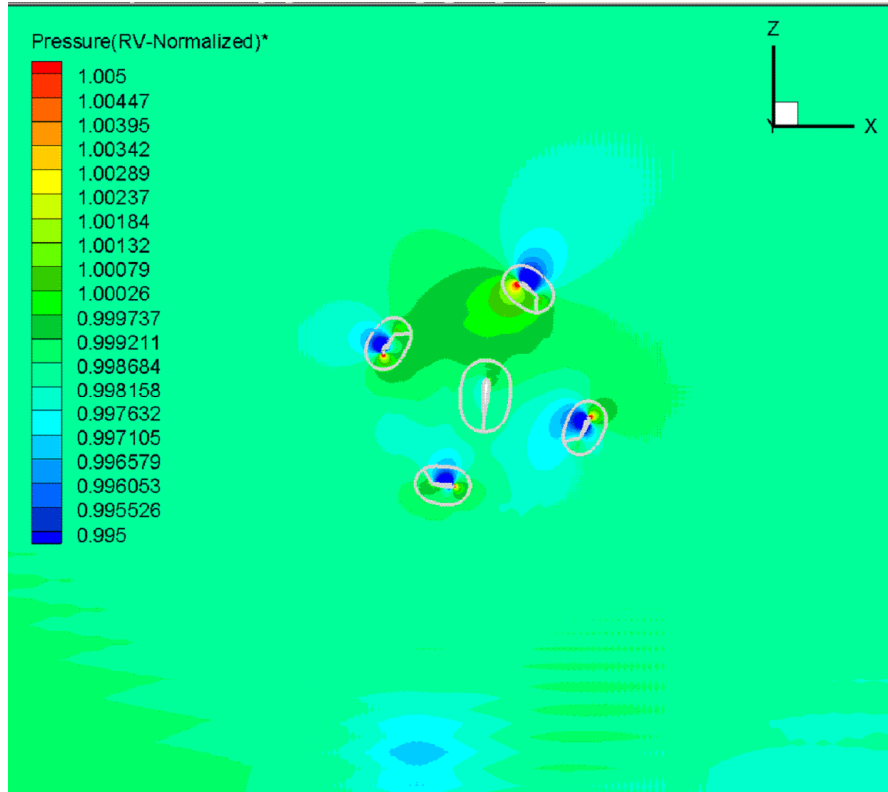


Figure 9. Pressure distribution in the rotor with blades lifting. Pressure in the jet is well matched to the ambient pressure.

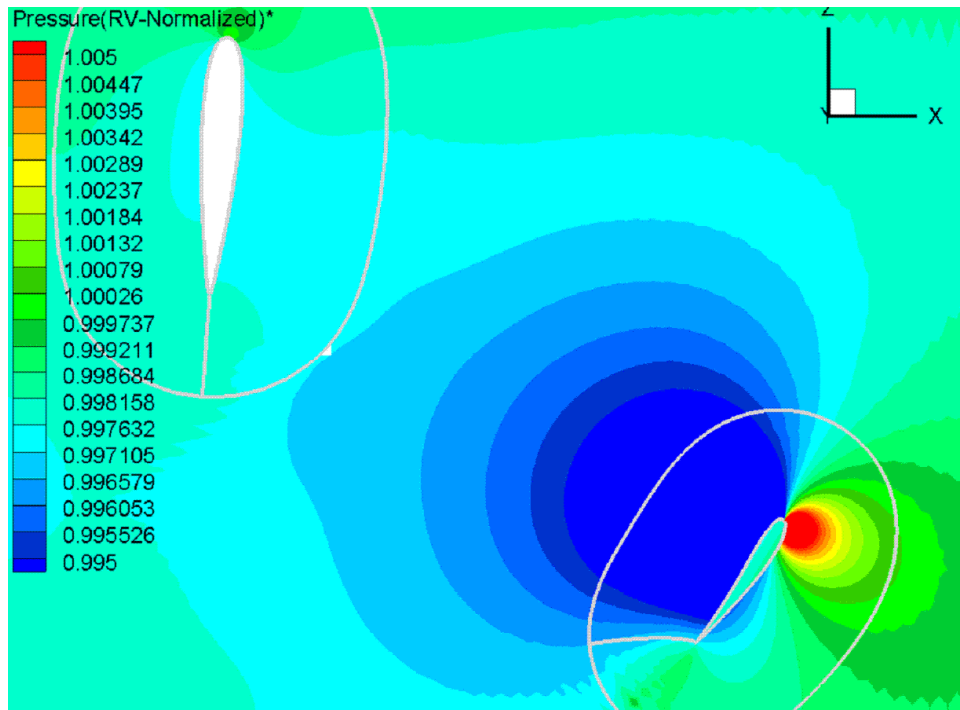


Figure 10. The source of the moment on the blade leaving the jet (310 degrees) can be seen.

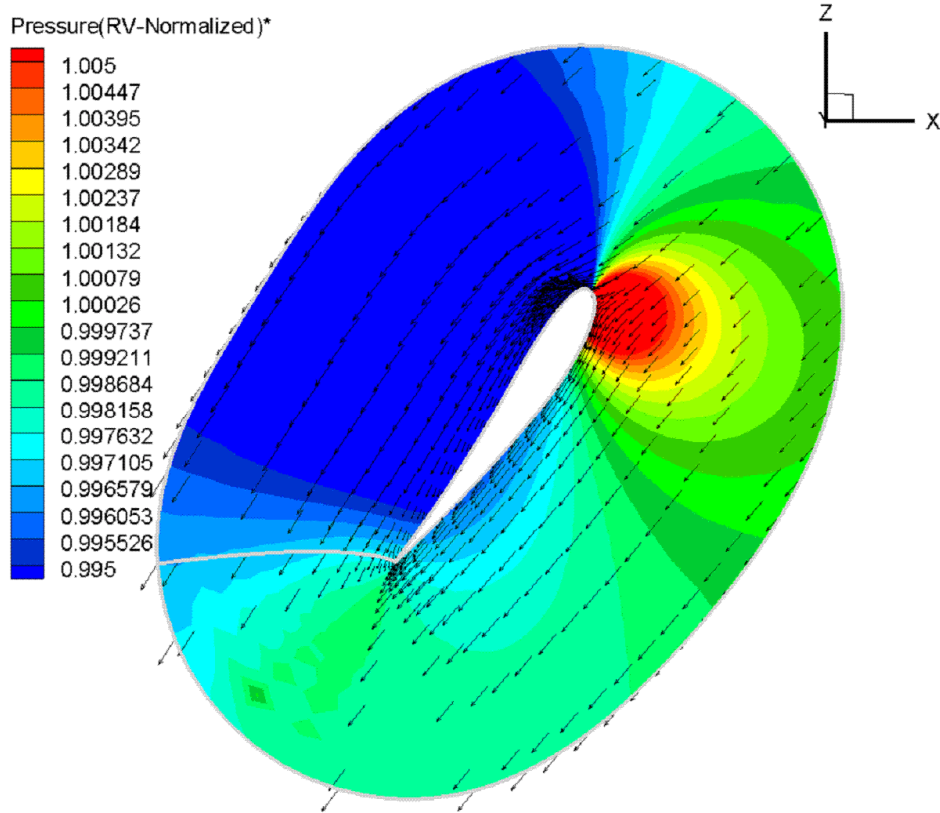


Figure 11. Pressure distribution at 310 degrees with blade-relative wind vectors. Although the stagnation point is well around the outside the flow appear to remain well attached, and the overall angle of attack is not extreme, as shown by blade-relative velocity vectors.

7.1.4.3 FOMOCO Results

While the blade images can provide useful intuition about the forces on the blade at a particular instance of time, the best visualization tool for the time-varying nature of the blade forces through a full 360 rotor rotation comes from the Overflow add-on tool FOMOCO. FOMOCO calculates Force and Moment coefficients on grid surfaces for each iteration by integrating the pressures around the surface of interest for every solution time point. The resultant graphs provide a good picture of the blade dynamics as a function of time.

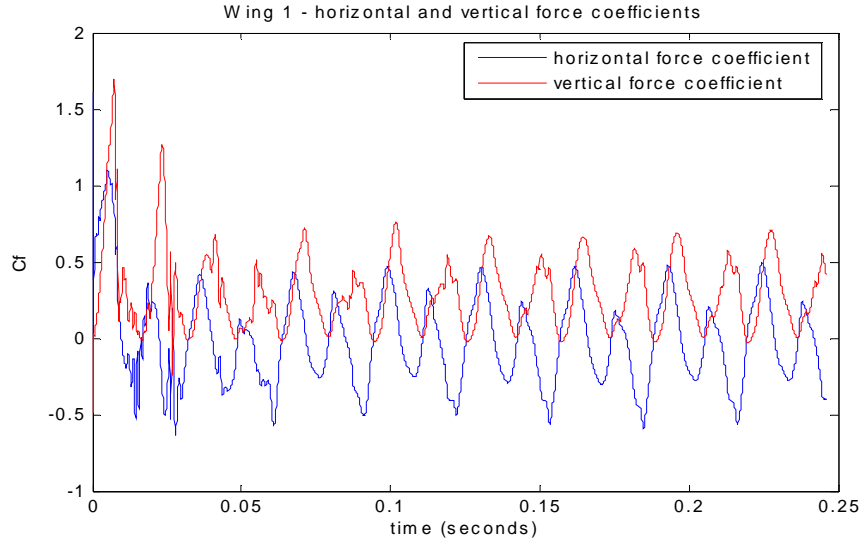


Figure 12. Initial startup force coefficients on Wing 1 followed by steady state behavior.

Figure 12 shows a FOMOCO output graph through several rotations of the main rotor. Note how the initial force spikes stabilize out as the jet reaches steady state after about four revolutions of the rotor. Even after steady state, one can notice the higher frequency signals in the vertical force coefficient as the blade passes through the jet. This behavior is more evident in the next figure.

Ideally, the force curves in the figure above would be perfect sinusoids thereby facilitating a smooth superposition of the forces. We will see in the next section that we were unable to completely cancel out the higher frequency ripples to produce perfect DC horizontal and vertical forces.

7.1.4.3.1 Force Superposition and Blade Profile Optimization

For smooth rotor performance, the sum of all the vertical and horizontal forces should be as close to constant as possible. Such perfect cancellation of the high frequency components would be possible if all four blades were producing sinusoids with a period equal to one full rotor revolution. The presence of the jet with its aforementioned high frequency temporal-spatial structures, such perfect sinusoids are practically impossible to generate with power constrained blade profiles. Thus there will always be some residual high frequency components in our superposition profiles. In particular, “optimizing” perturbations from previous profiles can introduce new or shift previous high frequency phenomenon negating the intended beneficial effect.

In practice, altering the profile of the blade as it “goes over the top” results in slightly fewer negative side effects but it still problematic. We found the best approach was to perform very small changes and to evaluate results before proceeding. For a profile limited to 9 fourier harmonics (due to the Overflow Fortran parser limit), profile tweaking reaches a point of diminishing returns. We present here the superimposed FOMOCO results.

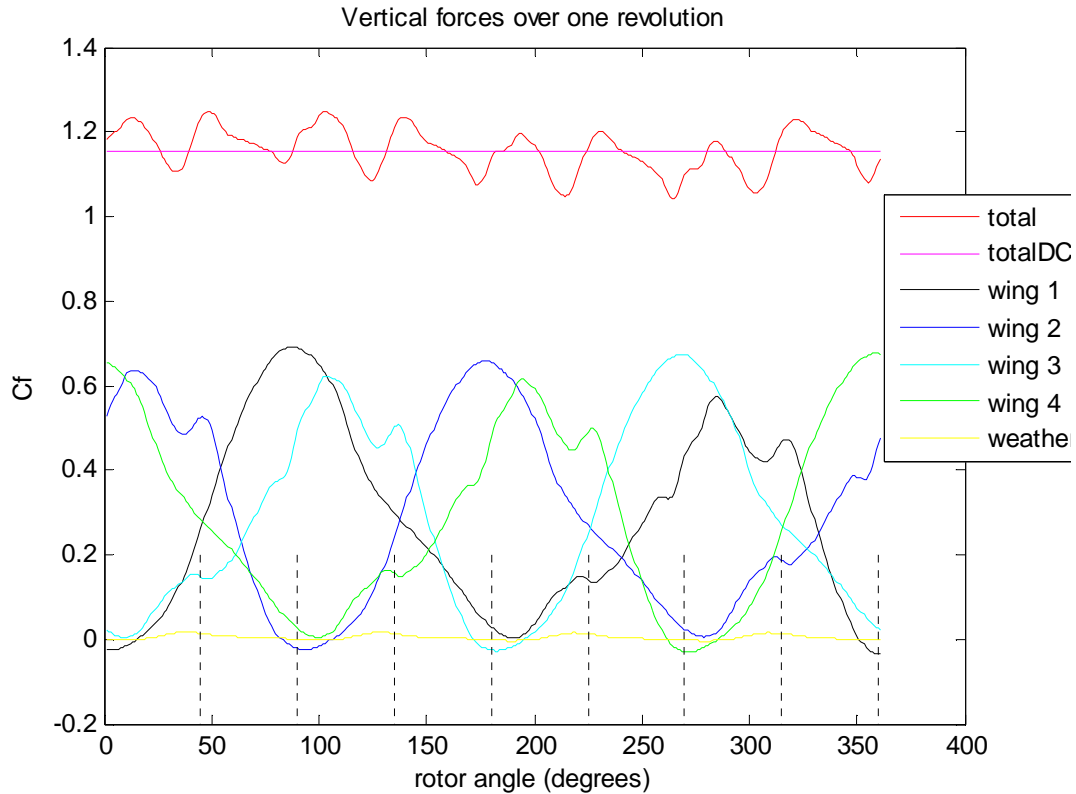


Figure 13. The superposition of the vertical forces from all four blades. Wing 1 is the blade profile discussed previously. Wings 2,3 and 4 lag by 90,180 and 270 degrees respectively. We have manually modified the entire blade profile to smooth out the total vertical force as much as possible.

The resultant 4-blade superposition output has ripple that is about 10% of the average value at a frequency 8 times higher than the fundamental rotor frequency.

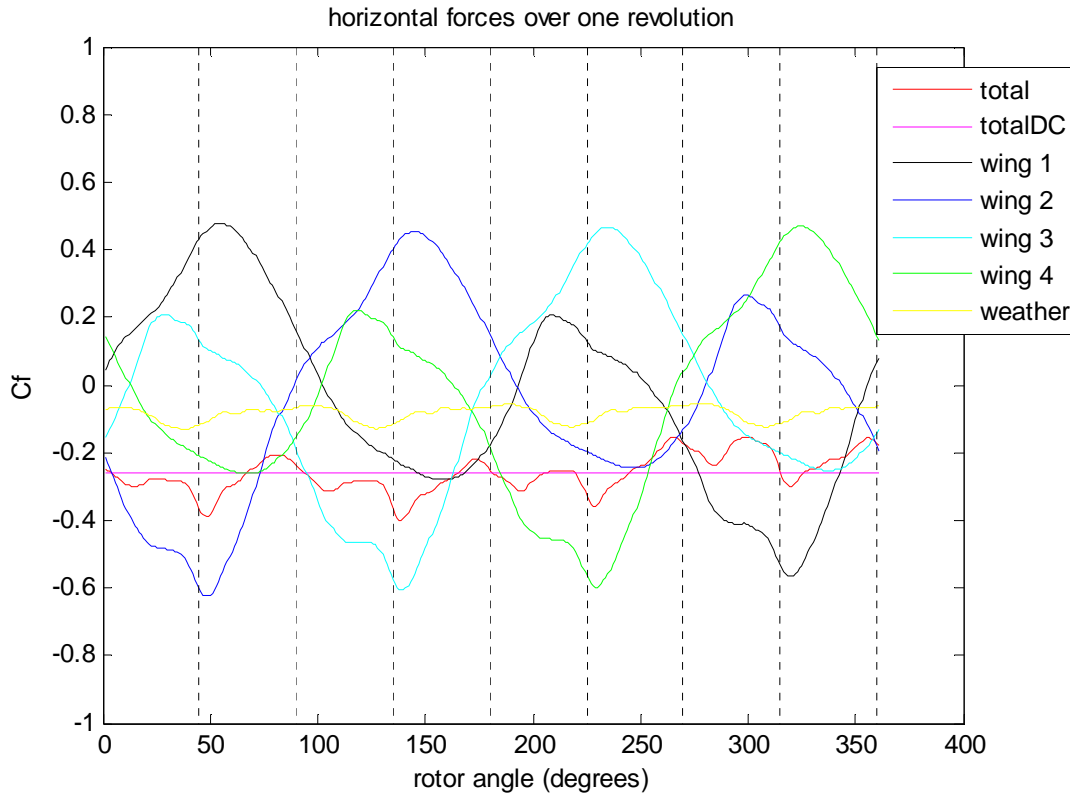


Figure 14. The superposition of the horizontal forces from all four blades. The ripple is similar in magnitude to that observed in the vertical direction although the frequencies in the ripple are lower.

The situation in the horizontal over one revolution is similar; the frequency content is somewhat lower in frequency and about the same amplitude of oscillation. There is an unintended bias in the horizontal force coefficient. Examining the curve for Blade 1, this appears to be originating in the 270-330 degree area - when the blade is cutting through the jet. The blade suffers from increased drag in this region and that is translating into a negative bias. The overall profile could be phase shifted to remove this unwanted component and to restore maximum lift.

Below are plotted the superimposed horizontal and vertical forces as a function of time showing the initial startup forces followed by the smoother steady state results.

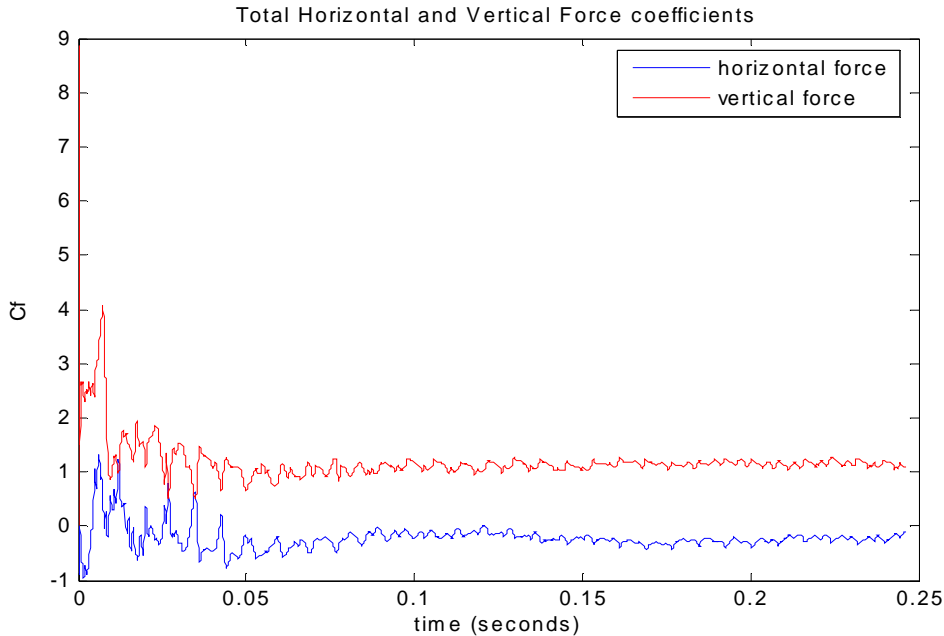


Figure 15. Total Rotor Force - Steady state performance of the superposition of all four blades.

The force coefficients are based on a reference speed of $M = .184$ (200 ft/sec), rather than actual speed so they are proportional to the forces, although blade airspeed varies around the rotor. The average vertical moment is 0.42 per blade, so the force per blade ft is 4.26 lb per blade ft. Figure 11 shows that some vibration remains. In Phase 2 an adaptive algorithm will be developed that continuously adjusts blade profile to minimize vibration.

In flight adaptive blade angle profiling will modify the blade angle profile in response to measured forces in real time. This may be needed to obtain the smoothest bench runs as well, since the true forces are not exactly predictable.

When the forces on the individual blades are plotted (Figure 16) it can be seen that while the force profile is fairly smooth over the top of a vertically lifting blade, substantial fluctuations occur as the blade passes through the wash from the upper blades in the lower rotor. This can be seen in the range from 210 to 330 degrees. At 0 / 360 the blade is moving vertically upward, and is at its lowest point at 270 degrees, as shown in Figure 6.

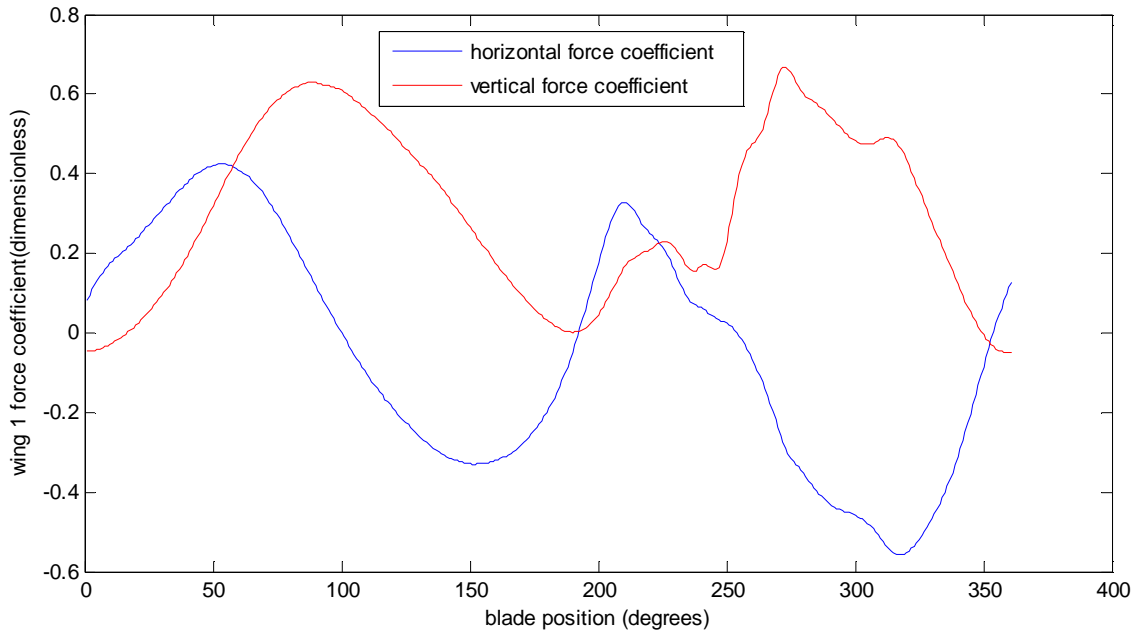


Figure 16. Horizontal and vertical force coefficients on one blade moving through 360 degrees. Note how the forces are smoothly varying during the top half of the profile compared to the bottom half where the blade is buffeted by the forces from the jet. The same jet forces produce the largest moments on the blade as the blade enters and leaves the jet (note the Cm graph behavior around 270 degrees).

Figure 17 shows the horizontal and vertical forces on one blade decomposed into radial and tangential force components. Power requirements are represented by the red line in Figure 17, showing the tangential forces on a blade in fTheta. (Negative corresponds to force input required) As expected power required to generate lift when moving through the fast jet at the bottom of the rotor will be quite high.

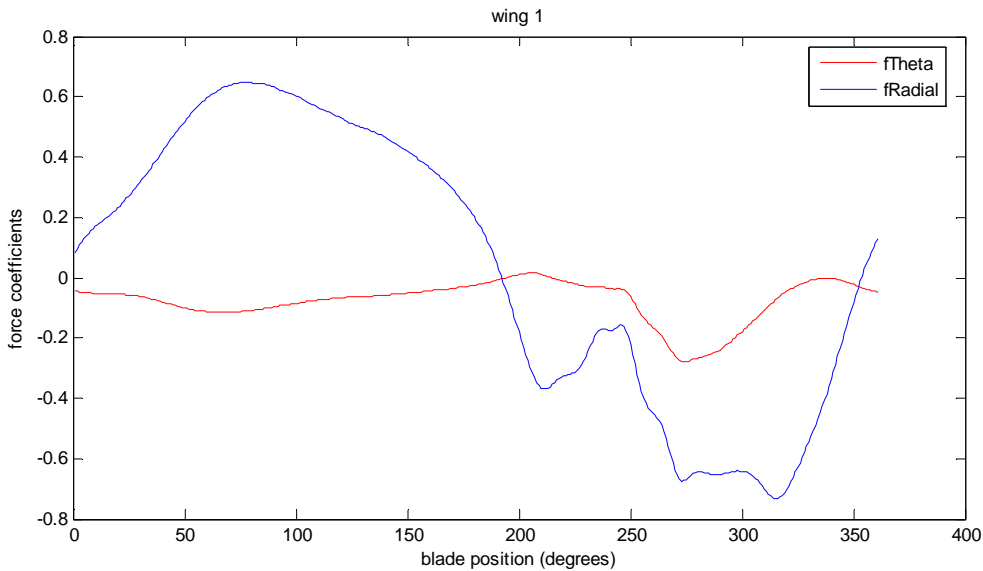


Figure 17. Force Coefficients resolved into radial and tangential components.

Blade Moments

The moments on a blade were also computed from the CFD results and are plotted in Figure 17. The positive peak to $+0.065$ followed by the negative peak for each blade are the result of the blade entering the high speed flow in the lower center of the rotor. The leading edge enters and leaves first, resulting in sharply varying external low conditions along the chord. On the upper half of the rotor, the moment magnitude is below 0.006 , as predicted from our airfoil design process.

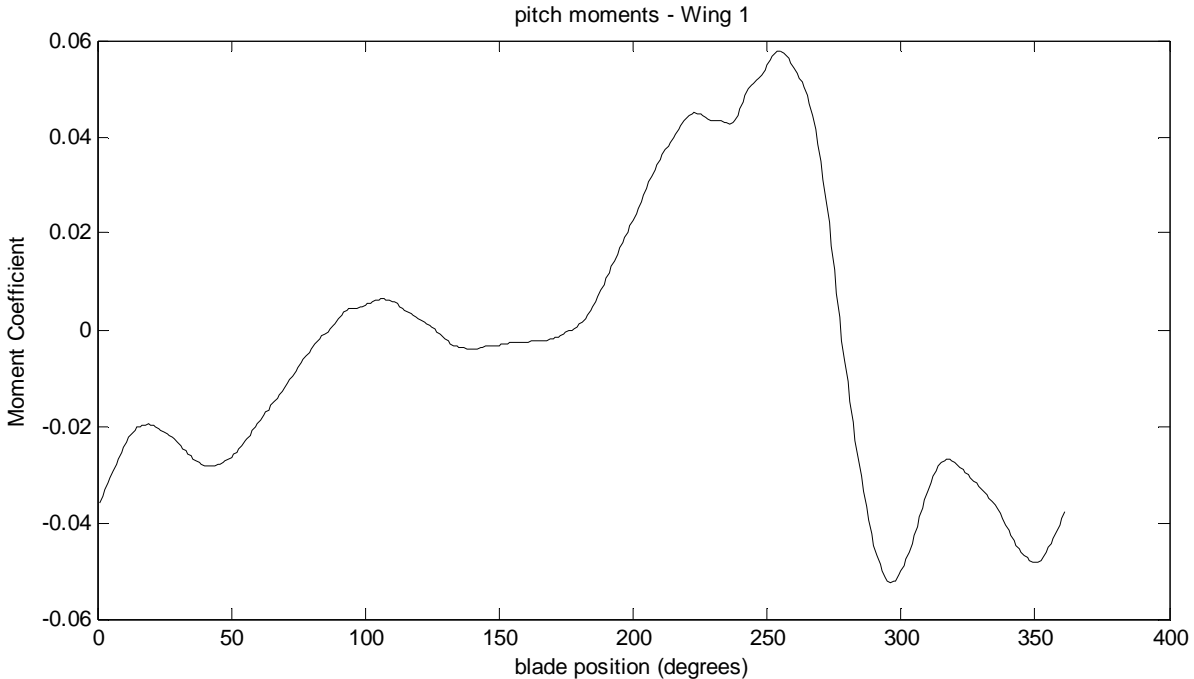


Figure 18. Moment coefficient at the blade axis, 0.23c.

This may pose a significant challenge to our blade attitude motors, since the desired direction of rotation at both moment peaks is in the direction to the moment. The blade motors are capable of 0.141 ft-lb of torque. A moment coefficient of $.06$ at 200 ft/sec and chord of 2.56 inches results in 0.130 ft-lb of torque required per blade foot, or $.324$ ft-lb per blade. Blade inertial is small relative to these forces. In the near future we will be investigating blade profiles which reduce the required torque and smooth out the lift and horizontal force fluctuations.

7.1.4.3.2 Forward Flight

While we have conceptualized some of the general characteristics for a suitable blade profile during forward flight, we have not yet optimized past our initial first order estimate of the profile. The figure below shows two wing configurations in an imposed 0.3 mach air stream. We have overlaid the two configuration to illustrate the general features of the motion. The most significant difference is that the blades “wind-up”, i.e. they must continually rotate to maintain a wind-facing profile throughout their rotation. In our analytical function this is accomplished by adding a constant velocity term in addition to the fourier terms. We will investigate the moving scenario further in Phase II research.

Extracting Effective Angle of Attack

Although the blade airspeed and angle of attack have not been extracted from the CFD data and are not well defined, we have backed out the effective angle of attack by getting approximate horizontal and

vertical airstream speeds around the rotor from the plotted output and approximating them with a 2-term Fourier series, shown in Figure 19.

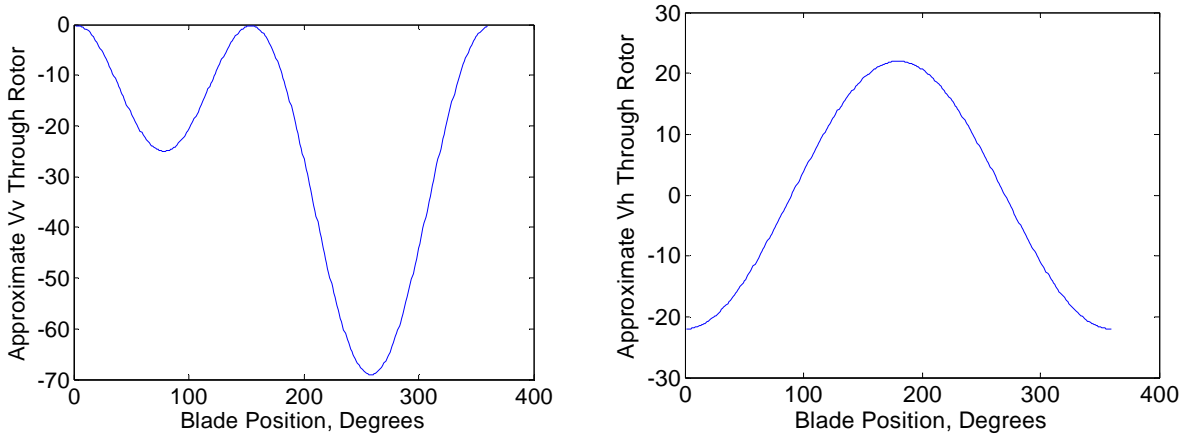


Figure 19. Approximation of effective stream airspeed vertical and horizontal components, encountered by a blade moving on the rotor.

From these and the force coefficients, an effective angle of attack is computed, making the rough assumption that form drag is 1% of total drag:

$$\alpha = .99 C_{Ftotal} / 2\pi,$$

where CF is the total force coefficient, α is blade angle of attack (radians) and .99 CF is assumed to be the lift coefficient, This results in the angle of attack profile in Figure 15. Since it does not model tip losses or nonlinear lift curve slope effects, the actual effective angle of attack range in the simulation would be slightly larger.

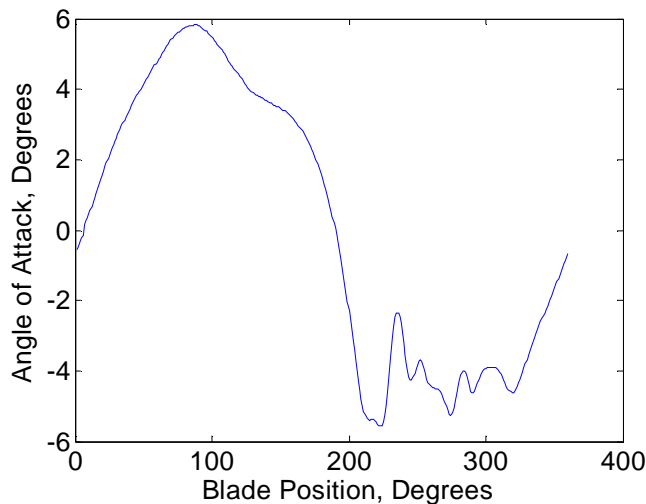


Figure 20. Effective angle of attack profile computed from 2-D lift slope.

This allows us to predict induced drag in 2 ways: with the blade aspect ratio of 12, and with the rotor aspect ratio of 1.25. Force and Power required for each is shown below. With the blade aspect ratio of 12, power is 0.247 lb within a few percent of the CFD derived power of 0.262 hp/blade ft, but rises to 0.45 hp / blade ft at a rotor aspect ratio of 1.25, each assuming an Oswald factor of 0.75. Power per rotor

ft required for each case is shown in Figure 21. We expect that actual power required will be between these values.

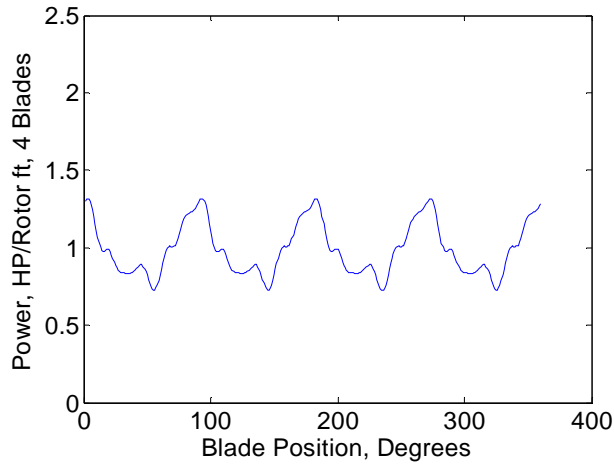


Figure 21a.
Power/rotor ft required for AR=12

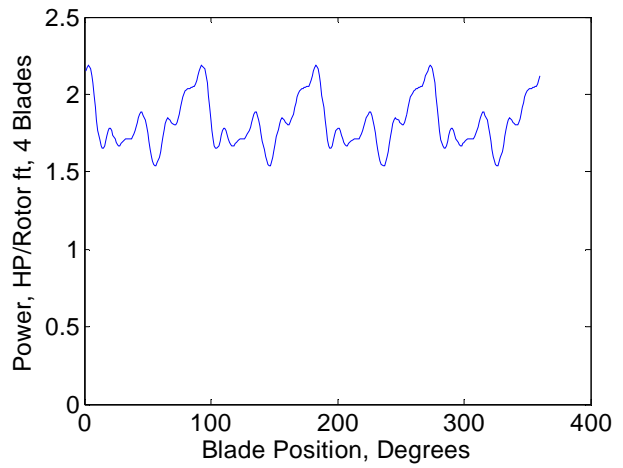


Figure 21b.
Power/rotor ft required for AR=1.25

7.1.5 Rotor and Test Stand Model

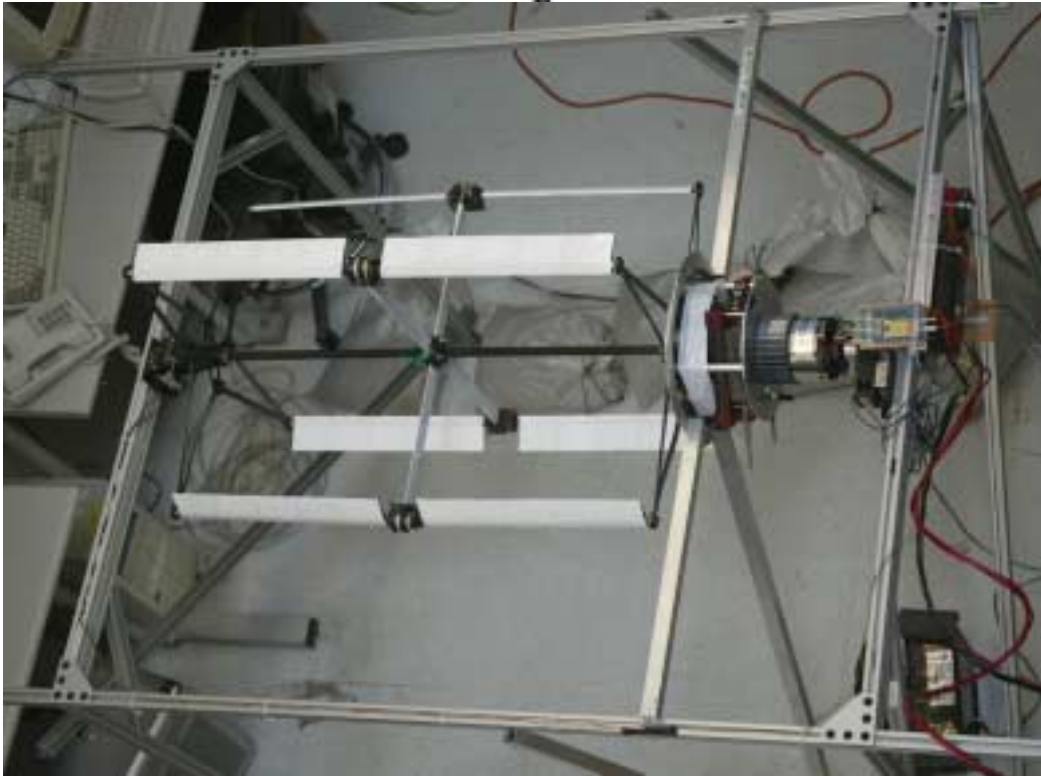
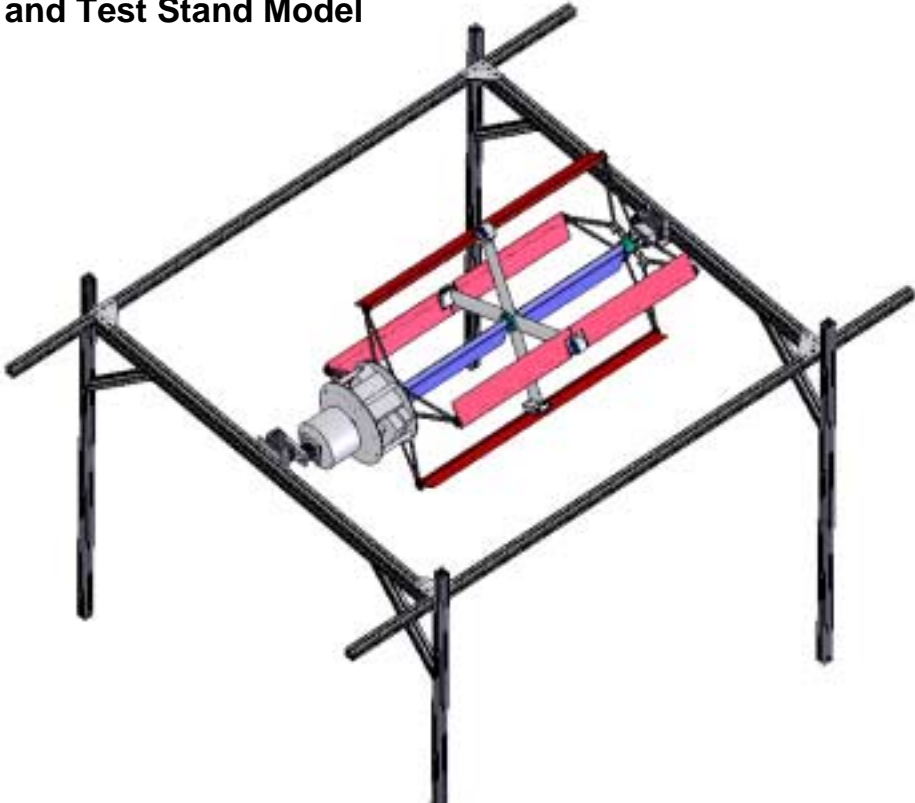


Figure 22. Rotor and Test Stand

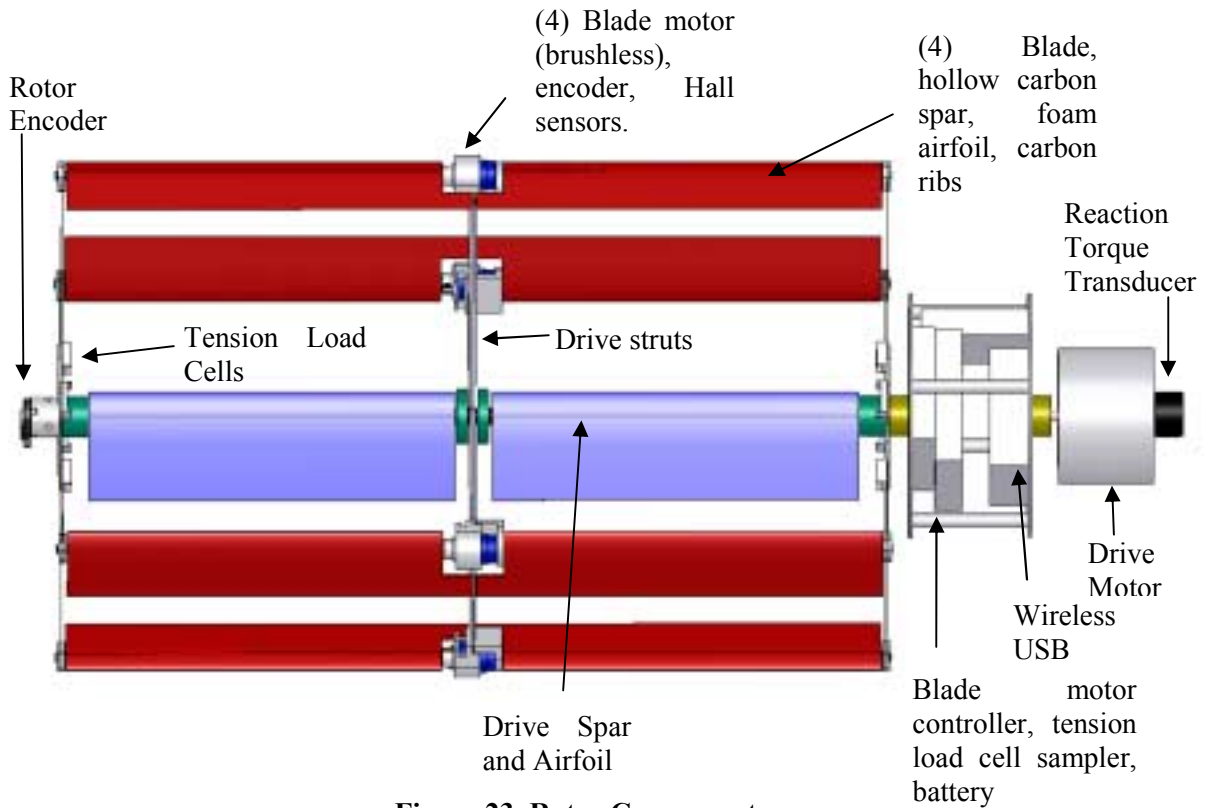


Figure 23. Rotor Components

Main Drive Motor

The main drive motor selected is a 15 hp brushless electric motor weighing 3.5 lb. It is run at up to 4 hp at 100 to 2000 rpm. Automobile batteries are used to provide the 24 Volts, 200 amps required. A speed controller designed for the motor was used with it.

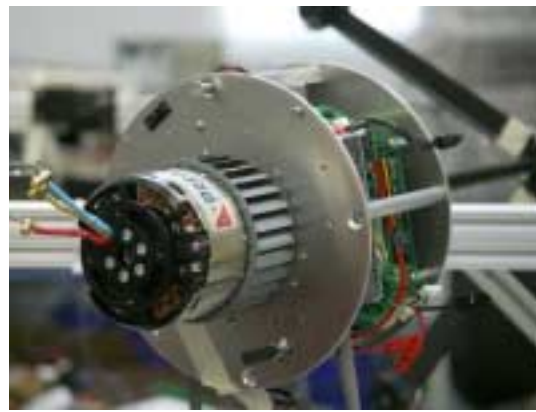


Figure 24. Blade Motor Servo Controller

Figure 25. Motor with Fan and Electronics Hub



Figure 26. Rotor Wiring.
Green Wires Were Used for Easy Color Identification.

7.1.5.1 Rotor Supports and Lift/Thrust Load Cells

The rotor ends are each supported on 2 linear slides and 2 load cells. The slides transmit torque to the frame and allow the load cells to pick up rotor lift and thrust. These are shown in Figures 27, 29 and 30.

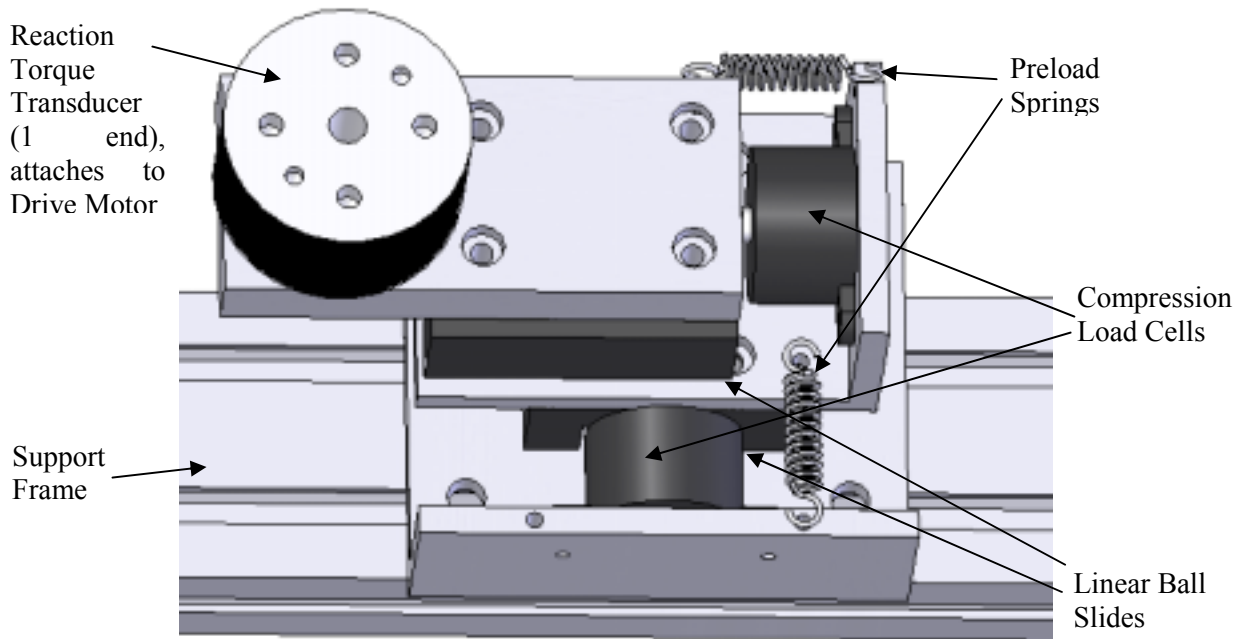


Figure 27. Frame attachment and load and torque cell mounting design.



Figure 28 Motor, Controller, Torque Sensor



Figure 29. Load Cells, Ball Slides Opposite the Motor



Figure 30. .007" Thick Tension Struts and Hub.

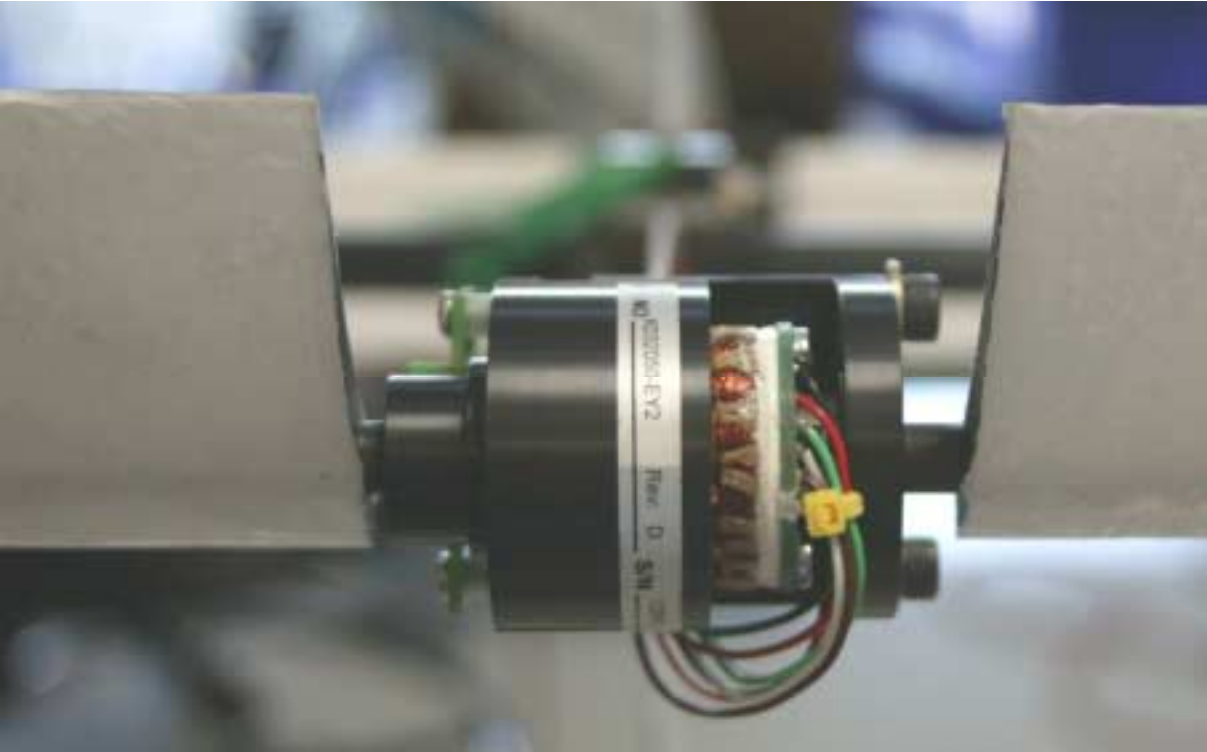


Figure 31 . Blade Incidence Angle Motor in Blade Center



Figure 32. Load Cell in Tension Strut



Figure 33. Tension Struts at Motor End of Rotor

7.1.6 Test Instrumentation and Parameter Measurement

An Ethernet based data collection device and an 802.11a wireless Ethernet hub were installed in the rotor hub with the blade servo controller, and powered from batteries. These provided 6 analog channels and 2

digital bytes of data at a 12,000 Hz sample rate. During testing, the main rotor shaft angle was measured and recorded from an 8192 count encoder of which the lower 7 bits were sampled. The blade angles were slaved to this encoder and were controlled with 4000 count encoders. The lower 7 bits of this was recorded. Motor index pulses were also recorded, but are usually missed at higher speeds. The blades are supported at their ends with pairs of tension spokes or struts as shown in Figures 32-33. Load cells were installed in two pairs of these at the end of the rotor opposite the main motor. The tension in one pair of these was recorded.

On the support frame, vertical and horizontal load cells were mounted at each end of the rotor. The rotor was constrained by crossed pairs of linear ball bearing slides to allow it to move against the load cells, and restrained against them with springs. At high speeds it was necessary to lock down one end of the rotor, so readings were taken only from load cells at the other end, and doubled to obtain performance numbers. The main motor torque was measured with a reaction torque sensor mounted between the main motor and the support frame. A Hall effect sensor mounted on the frame generated one pulse per revolution as a secondary rpm sensor, and to ensure main encoder count integrity at high speed.

All readings shown below have been scaled according to the load cell and torque sensor calibrations, and zeroed with the readings while stopped or at very low speed.

7.1.7 Test Results

After a number of shakedown runs and reattachment of various separated components, the rotor was run at gradually increasing speeds while data was collected. The phase of the blade angle profiles was rotated to direct the airstream horizontally out a roll-up door to avoid ground effects. The main motor was run on a 12 Volt car battery. Although it can accept up to 33 Volts and develop up to 15 hp, one battery provided adequate power for these tests.



Figure 24. Testing Blade Motors



Figure 35 Operating Rotor

Definitions

Terms used below in a manner specific to the cycloidal propulsion rotor are:

Coefficients of Force: Component of total force in a particular direction, expressed in dimensionless form. Directions used are **vertical**, **horizontal**, **radial** from the rotor center, **tangential** to the rotor rim, **lift** (vector sum of vertical and horizontal for a stationary rotor) and **drag**, the same as tangential.

Lift/Power: The lift produced (in lb) divided by the product of rotor speed in radians/sec and torque. Power is generally also converted to horsepower.

Rotor Loading: The lift produced (in lb) divided by the product of rotor diameter and length (in ft).

7.1.7.1 Rotor RPM and Motor Torque

Figure 36 shows an examples of rotor RPM measurements. A representative motor torque plot is shown in Figure 37. The torque spikes during acceleration, and has significant ripple due to the nature of the 20 pole main drive motor. For analysis, the torque was filtered with a 2nd order Butterworth filter to remove this.

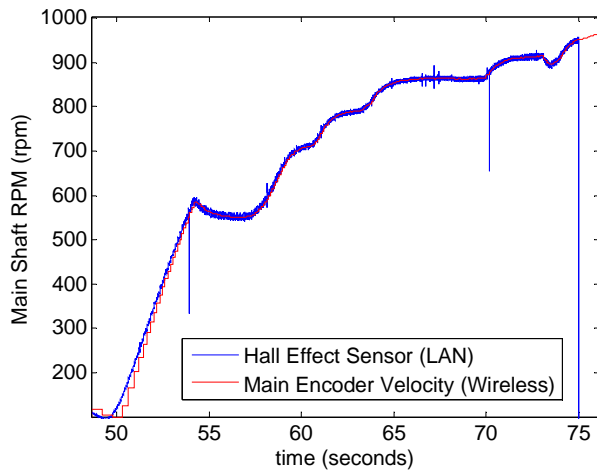


Figure 36. RPM, Encoder and Hall Sensor

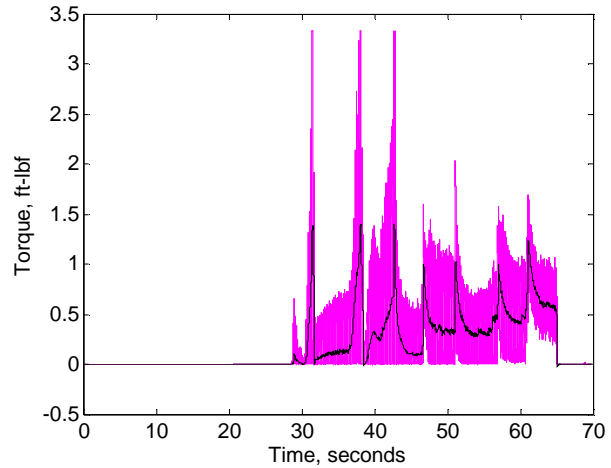


Figure 37. Motor Torque, Also Filtered Torque

7.1.7.2 Blade Tension

Prior to high speed operation, the attachment of the blades to the main shaft was tested by loading them with 50 pound sand bags at the support struts. This is the maximum load that was expected.

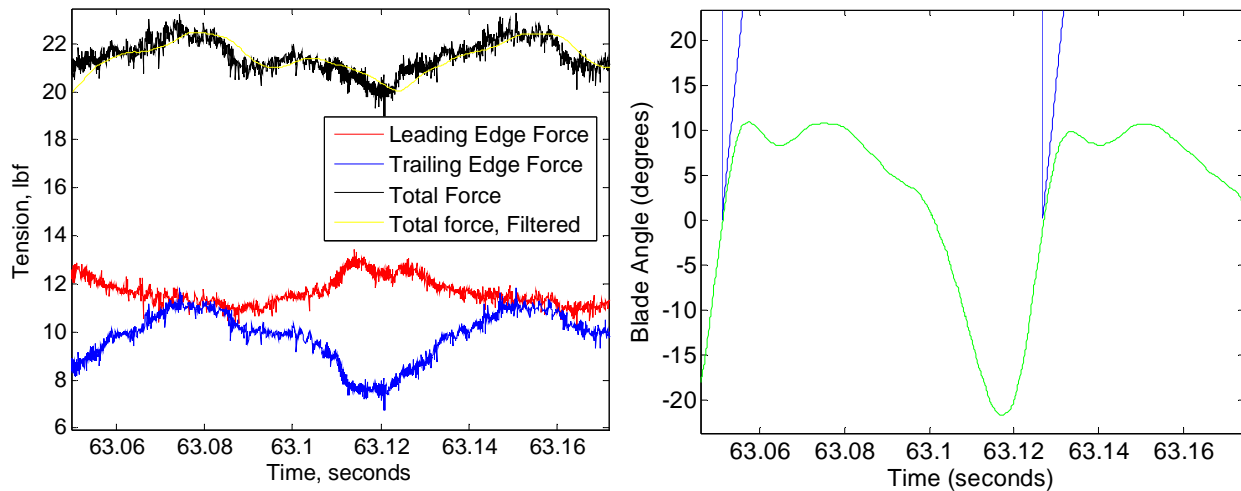


Figure38. Tension in Fore and Aft Blade Struts and Total Tension at 863 RPM

Blade tension at 863 rpm was 21 lb as shown in Figure 38. This was slightly more than expected, and would result in 112 lb at 2000 rpm. This is likely due to the addition of weight to the leading edges of the blades which was necessary to balance them at the support shafts. The fore and aft struts take varying amounts of load depending on the radial and tangential forces experienced by the blade, At 63.12 seconds, the load on the leading strut is highest, at the bottom of the rotor (in the jet), where the blade incidence angle is highly nose in toward the center of the rotor, and lift has the largest tangential component. At the same time the total force is a minimum, as lift generated counteracts the centrifugal force.

7.1.7.3 Lifting Forces

A representative horizontal and vertical force data set is shown with main motor RPM in Figure 39. The force data was examined by. For analysis, the data was filtered with a 2nd order Butterworth filter to remove this.

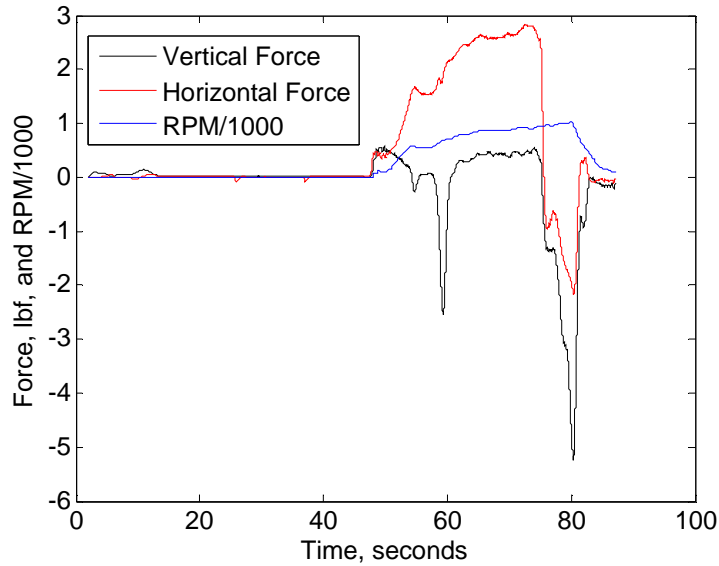


Figure 39. Lifting Forces and Rotor RPM

7.1.7.4 Parasitic Drag Determination: Fixed Angle Runs

Three data collection runs with fixed blade angles of -3, 0, and 3 degrees were performed to obtain the minimum drag incidence angle and drag coefficient. Figure 40 shows that minimum drag actually occurs at a nose in angle of approximately 5.9 degrees. This is a strong indication that our strategy of cambering the blades with the curve path of the rotor was inadvisable or overdone. Blade camber should be at least reduced, perhaps eliminated. This should be investigated further in future work. Since our rotor tests were run at a reference incidence of 0 degrees a slight penalty was apparently paid in excess drag: Wasted effort which would have raised the pressure in the center of the rotor. The foregoing assumes minimum drag does occur at zero lift or positive (outward) lift, which is likely given the camber.

.417 ft-lb @ 551 rpm at -3° incidence:
 - $C_D = .0549$
 .480 ft-lb @ 548 rpm at 0° incidence:
 - $C_D = .0638$
 .570 ft-lb @ 537 rpm at +3° incidence:
 - $C_D = .0790$
 $C_{D0} = .0520 @ -5.90^\circ$
 Drag at 863 rpm, 0° : 1.207 lb
 Power from Parasite Drag at 863 rpm, 0° : 0.200 hp

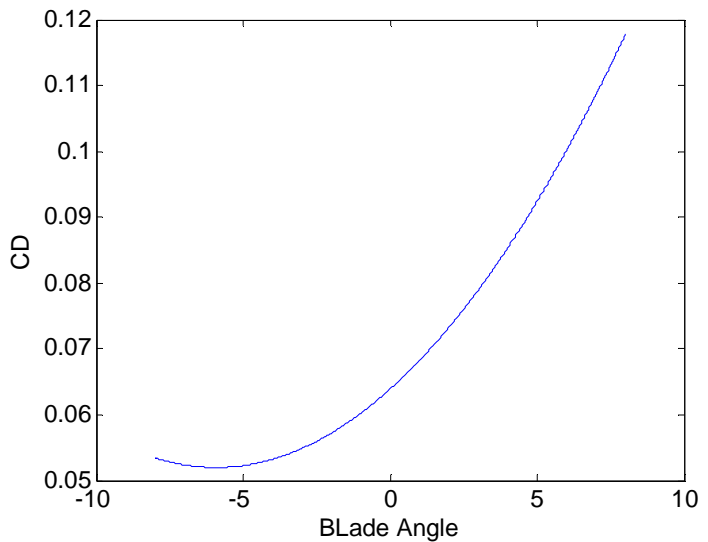


Figure 40. Data Points and Parabolic Fit for Minimum Drag Blade Incidence Angle

Moments on the blades were not measured directly. During the fixed blade angle runs, however, the blade angle was observed to shift nose out, as shown in Figures 41 and 42. The servo control loop had no integral term during our tests, and the blade angle was apparently responding to external moments. The tendency was strongest at -3 degrees, which suggests the possibility of a zero moment point, although not near the minimum drag angle of -5.9. The moment is likely a combination of blade mass imbalance, which would be always in the same direction for angles near zero, and aerodynamic forces which could be zero at some small incidence angle, depending on the accuracy of our identification of the center of pressure for small angles. One possibility is the combination of a nose out mass imbalance combined with a restoring aerodynamic moment centered near the minimum drag point.

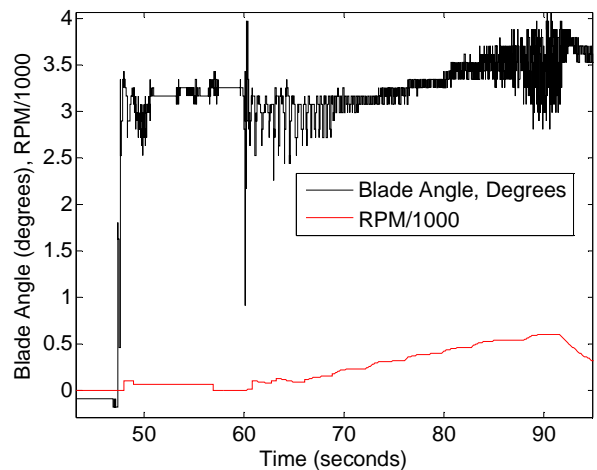
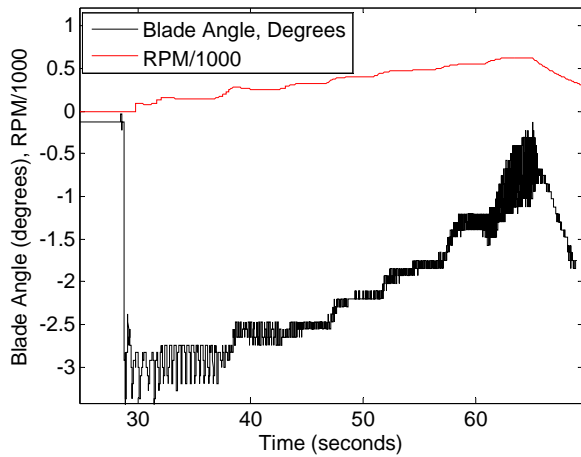


Figure 41. Blade Angle at initial incidence of -3° **Figure 42. Blade Angle at initial incidence of +3°**

Both aerodynamic and inertial forces increase with rotation rate squared, so separating them requires additional sensing. Our servo board is capable of sensing and recording motor torques, so this can be used to quantify the moment. Since we cannot easily separate the mass supported by the tip struts from the mass supported by the center strut, the lift generated for a given blade angle profile cannot easily be separated from the inertial forces, except from wing section theory or perhaps by inferring it from the varying blade angle run blade strut tension data. This will be investigated in future work. However, it is clear that the blades must be well balanced both inertially and aerodynamically to conserve servo effort for rapid angle changes at high speed.

7.1.8 Blade Forces

Figures 43 - 44 compare the radial force measurement from the blade tension load cells at 551 RPM with the blade incidence angle, the CFD result, and the computation from our phase 1 proposal. The CFD result has a more pronounced peak as a blade passes over the top of the rotor, and the trough as it passes across the bottom is narrower than the experimental data. This may be due to many effect, including tip effects, rotor vibration, and fidelity of the blade angle to the commanded angle. This points up the potential benefit of using an adaptive system in sensing and reducing residual vibration, as we will do in the future.

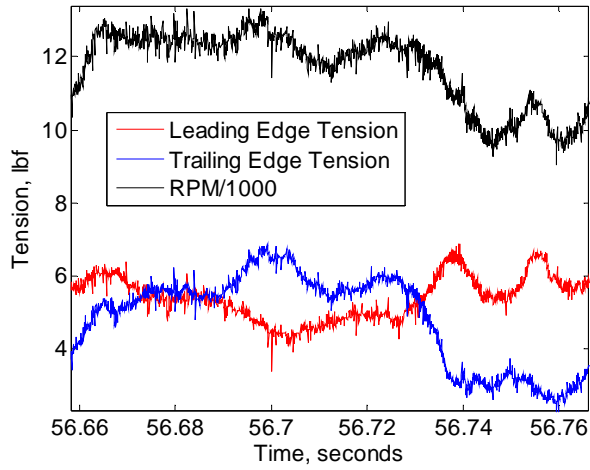


Figure 43a. Tension at 550 rpm

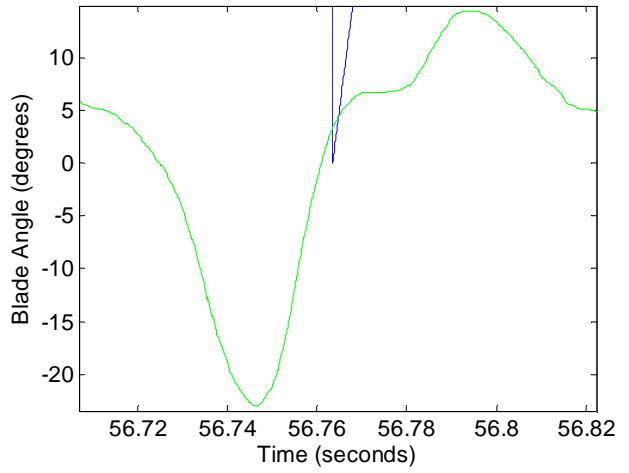


Figure 43b. Blade angle at 550 rpm

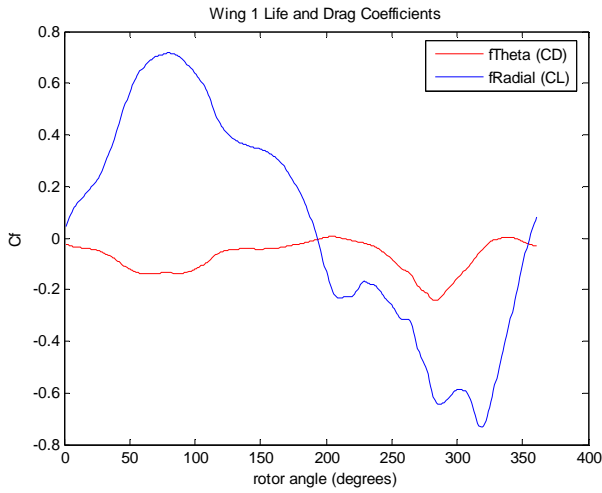


Figure 44a. CFD Radial Force (2D)

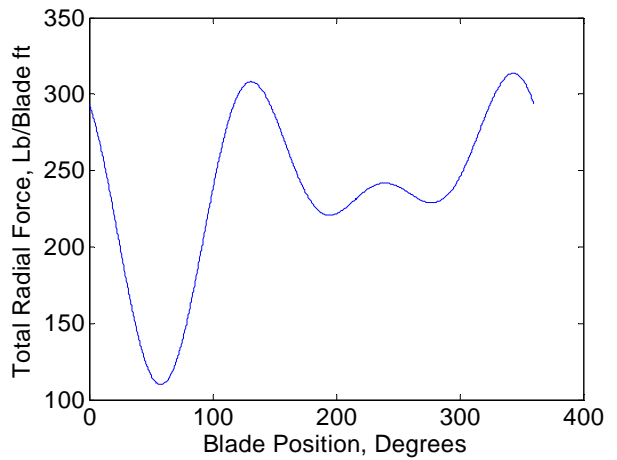


Figure 44b. Classical Aerodynamic (3D) Force Calc.

7.1.9 Results of Lift Measurement Runs

Figure 45 shows the data used to determine rotor performance. Lift, the vector sum from the horizontal and vertical load cells, is plotted with RPM and power, the product of torque and radians/sec, and lift/power ratio.

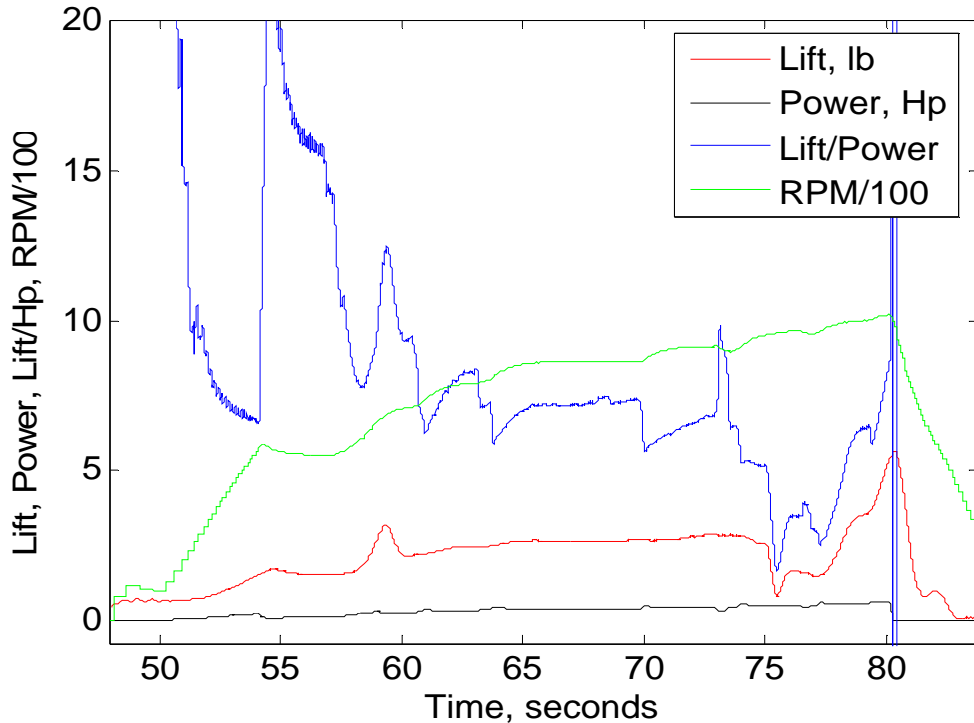


Figure 45. Performance Parameters

Several preliminary remarks about Figure 45 are in order. First, the data has been filtered to remove intra-cycle fluctuations and more clearly show trends. The increased ripple in Lift/Power at low rpm is the result of the filtering applied, which removes lower frequency per-cycle fluctuations less effectively than at high speeds.

It can be seen that during periods of increasing rpm, the lift and power are both higher than at steady state for the same rpm. The lift is higher since the air flow through the rotor is below its steady state speed, and the blades are therefore more effective. Power is higher due to the work needed to accelerate the rotor. When RPM is decreasing, the reverse are true. Therefore, performance metrics are only valid after constant RPM has been reached.

Two areas of constant RPM are analyzed here. The first occurs at 551 rpm, at 57 seconds. The second occurs at 963 rpm, at 67 seconds. This time is spanned by Figure __. Other brief periods of constant RPM can be seen in Figure __, at 60.5 seconds and 63 seconds, but these fall between the points analyzed in all respects. The increased ripple in lift/power at low rpm is the result of the filtering applied, which removes lower frequency per-cycle fluctuations less effectively than at high speeds.

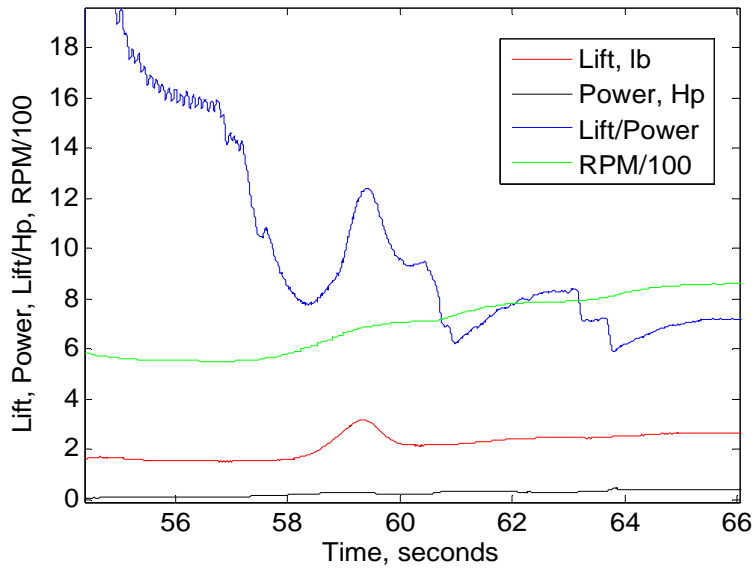


Figure 46. Performance Parameters from 550 to 865 RPM

7.1.9.1 Lift to Power Ratio

Lift/Power generally falls with increasing RPM, as it does with all static rotors and propellers. However, between 56 and 67 seconds, where speed goes from 550 to 860 rpm, there is significant rolloff in the response envelope of the blade angle, and lift to power suffers accordingly, dropping from 15.75 to 7.14 lb/hp. This is shown in Figure 46. Since for static rotors and propellers lift/power drops linearly with rpm for constant blade angle profiles, a 36% reduction would be expected. The drop 55% is most likely due to the decay of the quality of the blade angle profile, particularly over the top of the rotor where blades can most efficiently develop lift. Another energy sink may be the gradually increasing vibration that was observed at increasing RPM. Refined construction and balancing of rotors should reduce this considerably, as there was little work done on this in Phase 1.

7.1.9.2 Blade Angle Servo Accuracy

At 56 seconds, (551 rpm) the blades were following their angle profile more accurately than at 863 rpm, as shown in Figures 47 and 48. This is most likely due to the rolloff in the motor P-D control for the higher frequency components present in the shoulders in the commanded angle. In future work precompensation will be applied to the commanded position, and a more sophisticated transfer function for motor control will be used.

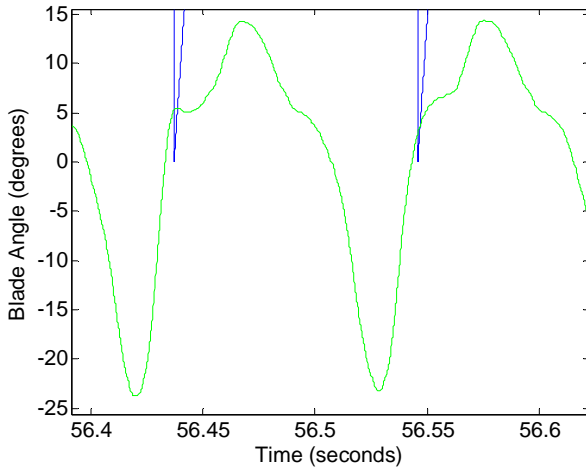


Figure 47. Blade angle from encoder at 551 rpm

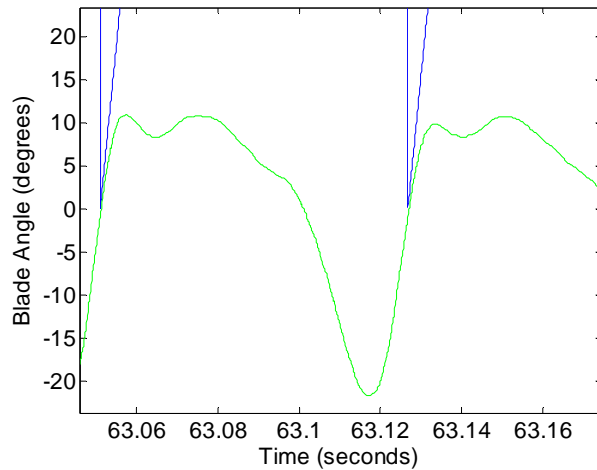


Figure 48. Blade angle from encoder at 863 rpm

7.1.9.3 Performance At Two Speed Points

Tabulated below are performance parameters for the 2D CFD runs and for the experimental runs with the phase 1 rotor.

2D PREDICTED, at 863 RPM Based on Coefficients from CFD runs at 1910 rpm (200 ft / sec)

Blade Angular Excursion, Peak-Peak: 41 degrees

Re (basis for coefficients): 450,000

Vertical Force: $C_{fv} \times q \times S_w = 5.465$ lbf

Horizontal Force: = 1.235 lbf

Total Force, 2D Blade: = **5.603 lbf**

Tangential Force: 1.376 lbf

Power, 2D Form and Skin Drag: 0.227 hp

Lift/Power, 2D Blade @ 863 rpm = 24.68 lb/hp

MEASURED, 551 RPM

Re: 130,000

Blade Angular Excursion, Peak-Peak: 39 degrees

Vertical Force: 2.62 lb

Horizontal Force: .476 lb

Total Useful Avg Force: **1.530 lb**

CL rotor blades: 1.530 / (q Sw) = .2013

Torque: 0.930 ft-lbf

Power: $57.70 \text{ r/s} \times 0.930 = 0.097$ hp

Power to Parasite Drag: 0.049 hp

$CD_i = \text{Drag} / (qSw) - CD_0 = 0.0586$

Lift/Power = 15.75 lb/hp

Lift/(Power from Drag Due to Lift): 31.88 lb/hp

MEASURED, 863 RPM

Re: 203,000

Blade Angular Excursion, Peak-Peak: 33 degrees

Vertical Force: 2.62 lb

Horizontal Force: .476 lb

Total Useful Avg Force: **2.663 lb**

CL rotor blades: 2.663 / (q Sw) = .1428

Torque: 2.205 ft-lbf

Power: $91.00 \text{ r/s} \times 2.205 = .364$ hp

Power to Parasite Drag: 0.200 hp

$CD_i = \text{Drag} / (qSw) - CD_0 = 0.0545$

Lift/Power = 7.139 lb/hp

Lift/(Power from Drag Due to Lift): 16.24 lb/hp

7.1.9.4 Blade Angle Precompensation at High Speed

One run was made using a simple precompensated blade angle profile based on blade step function response. The blade response Z-domain transfer function was first modeled as a fourth order system

from the step response data shown in Figure _ using the Steiglitz-McBride iteration tool in the Matlab Signal Processing toolkit. This gave

$$H(z) = B(z)/A(z) = \frac{0.8501 - 3.3976z^{-1} + 5.0928z^{-2} - 3.3933z^{-3} + 0.84794z^{-4}}{1 - 3.9999z^{-1} + 6.0005z^{-2} - 40013z^{-3} + 1.0007z^{-4}}$$

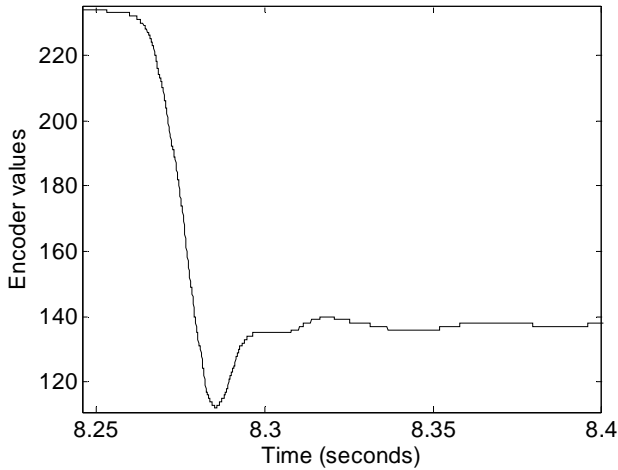


Figure 49. Blade step Response Measurement

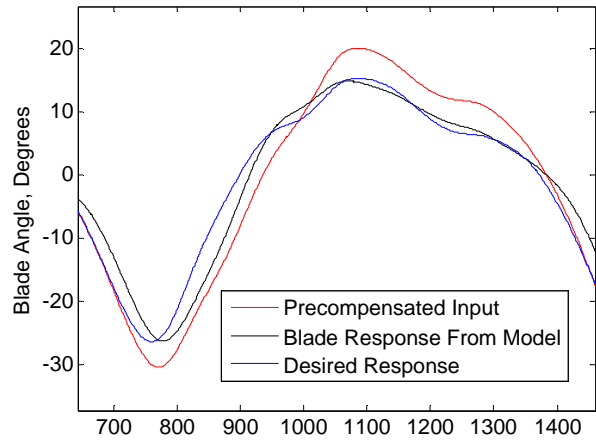


Figure 50. Precompensation

The impulse response of this transfer function was then deconvolved to obtain a precompensation blade profile. This is shown in Figure 50 with the desired profile and the anticipated blade profile at 863 Hz. No performance data was obtained from precompensation runs but a measured blade angle profile at 850 and 1075 RPM in which a top speed of 1175 RPM was reached is shown in Figures 53 and 54 .

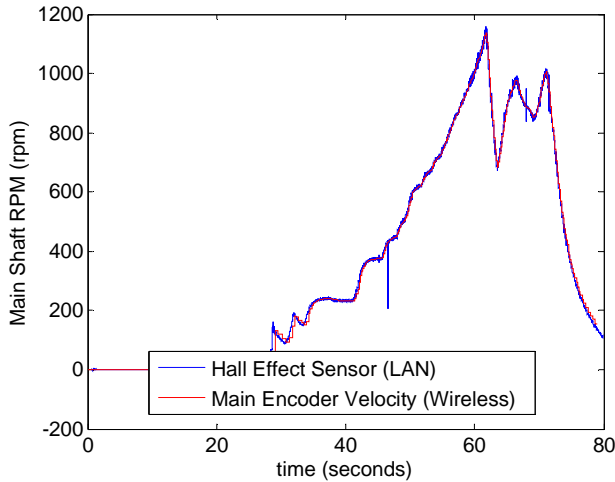


Figure 51. RPM During Precompensation Run

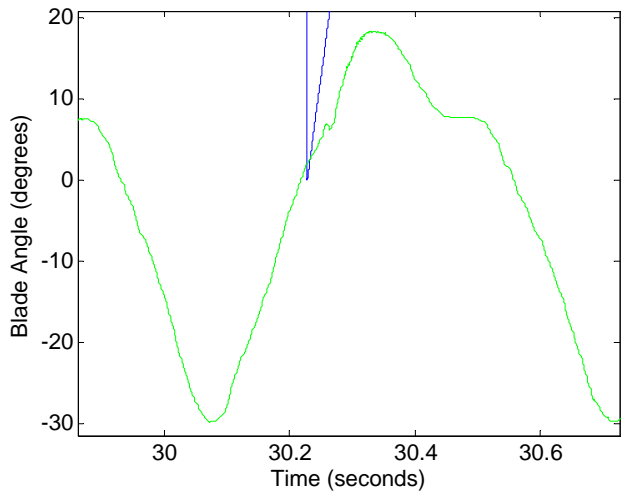


Figure 52. Blade Response with Precomp, 120 RPM

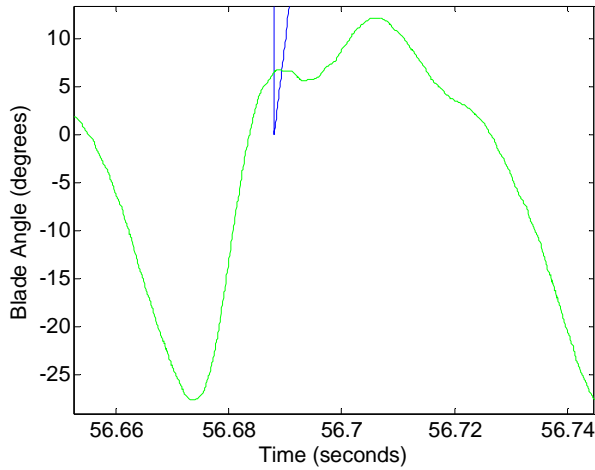


Figure 53. Blade Response with Precomp, 863 RPM

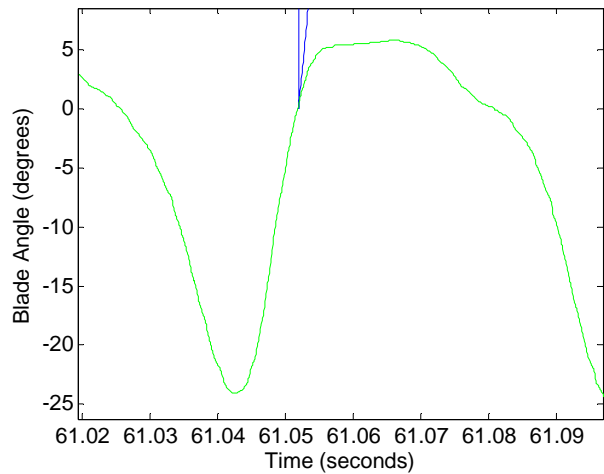


Figure 54. Response with Precomp, 1075 RPM

At low RPM, the blade profile tracks the input precompensated profile, with total excursion of nearly 50 degrees. The At 863 RPM, the blade profile was close to the desired profile, as this was the design speed for the precompensation. At 1075 rpm, the profile has decayed in a manner similar to the decay at 863 rpm without precompensation.

In order to track our commanded profile well, we initially used stiff servo gains with significant overshoot, making accurate precompensation difficult. If precompensation is used this stiffness is not necessary, as the servo response is modeled in the precompensation process. In an adaptive system where blade angle profile is changed in response to desired aircraft behavior, fixed profiles will likely serve only as general starting points, and precompensation design for every speed will be unnecessary.

7.1.9.5 Maximum Speed Reached

The fastest rotation rate reached was 1175 RPM, with the torque sensor amplifier reaching its upper rail. The horizontal and vertical load cells also hit their limits due to vibration. High end speed was limited by central shaft vibration which likely resulted from imbalances and shaft flexibility. This fell within our range of goals for phase 1, which were speeds of at least 1000 rpm and up to 2000 rpm if possible.

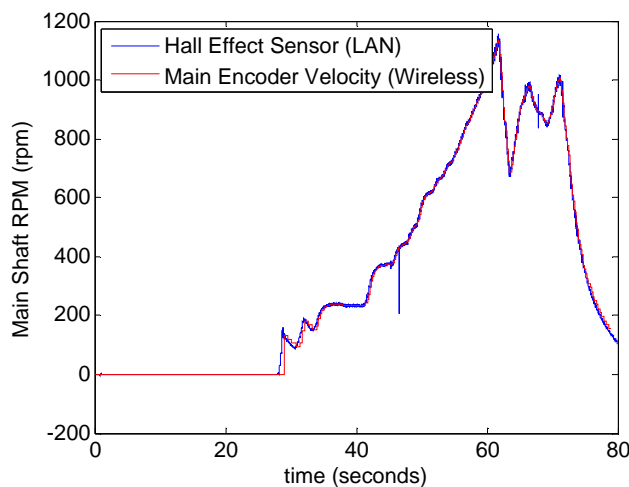


Figure 55. Maximum Speed Reached

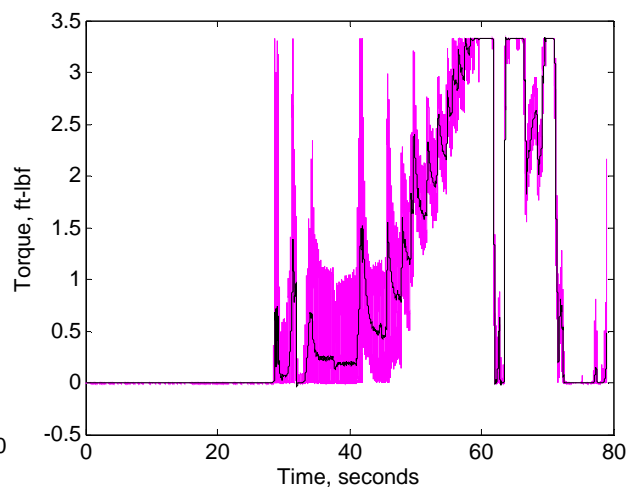


Figure 56. Torque at High Speed

7.1.9.6 Discussion

Rotor Coefficients of Drag and Induced Drag

The coefficient of drag due to lift is calculated from total drag and the zero lift drag coefficient obtained from the constant angle runs. For 551 rpm, we obtain $CD_i = .0586$. For 863 rpm, it is $.0545$. This is probably not too far from optimum for good lift to power, given the CD_0 of $.0638$.

Rotor Coefficient of Lift

The useful Cl of the rotor was predicted to be $.2936$ (the vector sum of the vertical and horizontal force coefficients $.2863$ and $.0653$) from the 2D CFD runs. The actual values obtained are $.2013$ at 551 RPM and $.1428$ at 863 RPM, or 72% and 49% of 2D modeling results. The differences can be ascribed to 3 factors:

3D Effects: Induced Drag

The third factor in the between the prediction and results is the difference between the 2D simulation and the 3D rotor. For fixed wings, best L/D occurs when induced drag equals parasitic drag, so a reduction of at least 2 in Lift/Power for a given RPM can be expected relative to the 2D result. Also, reduction in section Cl near the tips is likely significant, particularly since this rotor has wide breaks in the blades at the center where the motors are mounted. This effectively doubles tip losses. In future rotors, the motors may be moved to the central shaft; if not, a fairing that maintains the same Cl as the blade will enclose the motors. As with increasing Re, improvement would be seen primarily in power consumption, but also noticeable in lift produced.

Blade Angle Tracking Accuracy

The second factor in the difference between the prediction and results is the degradation of the blade angle profile at higher RPM, discussed above and shown in Figures 47 - 48. This is likely responsible for most or all of the loss of 32% in lift coefficient between 551 and 863 rpm.

Reynolds Number

Reynolds number effects were not taken into account. Reynolds number at 1910 RPM is 450,000, and at 863 rpm it is 203,000. At 551 rpm it is 130,000. We expect to operate at 300,000 to 450,000 or above with the phase 2 flying model. In a manned cyclogyro it would be around 2 million. Since wing performance improves substantially between 130,000 and 450,000, we expect that with appropriate blade actuation we will see performance at least as good as with the values at 551 rpm. This will be more noticeable in the lift/power ratio, but lift should also improve slightly.

7.1.9.7 Power lost to Parasitic Drag

The parasite drag used above is the drag at a blade incidence angle of zero degrees, which was the reference angle for the run. If the blade is operated at a minimum drag reference angle and the parasitic drag lowered by 50%, which should be achievable with shrouds and reduced rotor-based mass, the performance can be significantly improved over these first test results.

The power lost to parasitic drag at 551 RPM relative to power lost at 863 RPM should be proportional to the cube of the speed, or $(551/863) = 3.87:1$. Figure 57 shows power lost to parasitic drag obtained from our fixed blade angle runs. In fact, $3.87 \times 0.049 \text{ hp} = 0.190$, which is quite close to the 0.200 parasitic hp measured at 863 rpm.

7.1.9.8 Estimation of Higher Speed Performance

The performance of a cycloidal propulsion rotor of the same dimensions at higher rpm under various assumptions can be estimated. We assume here that the blade angle profile can be maintained at a quality

equal to that obtained at 550 RPM using appropriate motors and compensation in the servo controller. We also assume that parasitic drag can be reduced to 50% of present values through a combination of rotor cleanup and blade airfoil camber and reference incidence angle optimization.

We use lift, induced drag, parasitic drag, and power coefficients obtained as follows to generate the curves in Figure 57. This is for the blade angle profile from our CFD runs, which has not yet been optimized for lift/power. Expected improvements for full size rotors due to increase in Re to approx. 2M, and eliminating the gap in the center of the blade, are also not included.

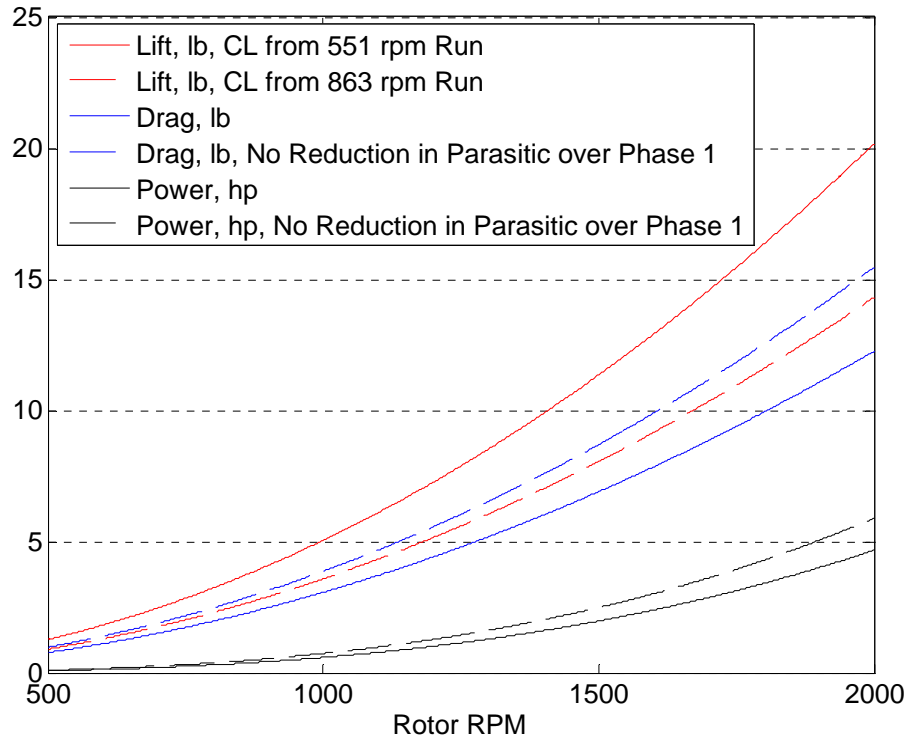


Figure 57. Lift, Drag, and Power for Flying Model Based on Phase 1 Results

We see that at 2000 RPM the lift per rotor is expected to be 14 to 20 pounds, depending on the quality of the blade angle profile. Based on a rotor projected area of 5 square feet, the rotor loading is 4 lb/sf. Lift to Power is expected to be approximately 4 lb/hp. This is well within the range of 30 pound model aircraft, and the 15 hp 3.5 lb motor used in Phase 1 could power one or both rotors on such a model.

7.1.9.9 Full Size Rotor Performance

For a prediction of full size blade performance based on phase 1 results we change the blade chord to 1 foot, the rotor diameter to 8 feet, and the rotor length to 10 feet.

We assume the induced drag coefficient of .0565 from the phase 1 measurements holds, using the same blade angle profile. Results are shown in Figure 58. In this case the parasitic drag is more important, but structure drag reduction in a larger vehicle should be feasible. In addition, increase in Re from around 200,000 to 2 million should improve blade performance.

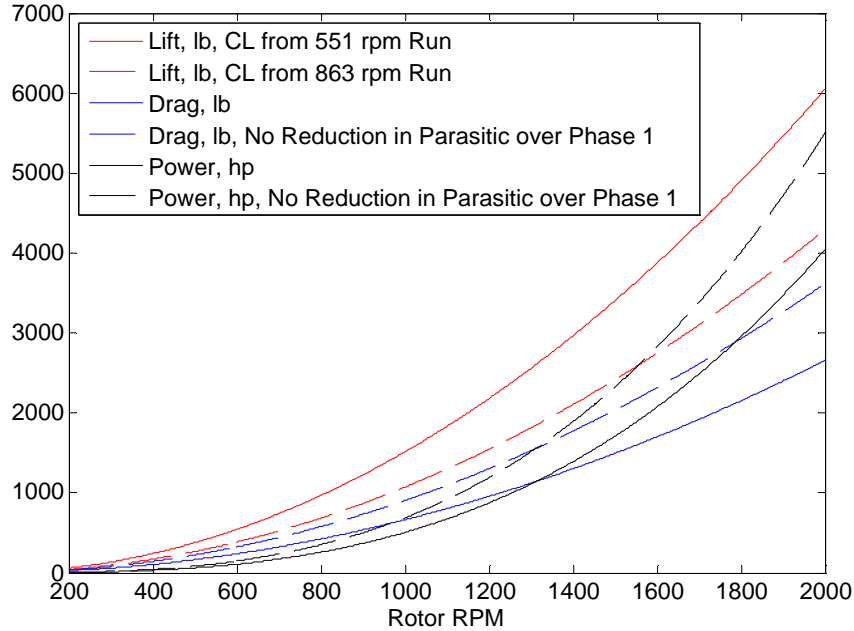


Figure 58. Lift, Drag, and Power for Full Size Cyclogyro Based on Phase 1 Results

This rotor has projected area of 80 square feet. Referring to Table 1 from our Phase 1 proposal, the disk loading of a Robinson R22 Beta II helicopter is 2.75 lb/sf. At this projected rotor area loading of the lift would be 220 lb. From Figure 58 the rotor speed would be 381 RPM and the power would be 28.1 hp. This is a power/lift of 0.127 hp/lb, the same as the Beta II value of .13 hp/lb at the same loading.

The disk loading of a Bell 407 helicopter is 5.71 lb/sf. At this projected rotor area loading of the lift would be 457 lb. From Figure 58 the rotor speed would be 550 RPM (coincidence) and the power would be 84.1 hp. This is a power/lift of 0.18 hp/lb, compared to the Bell 407 value of .12 hp/lb at the same loading.

Vehicle	Weight/Load	Rotor Area	Disk	Disk/Rotor Loading	Lb / SHP @max weight
Robinson R22 Beta II	1370 lb	497 sf		2.75 lb/sf	.13 shp /lb
Bell 407	5500	963		5.71	.12 shp /lb
NACA Cyclogyro Prediction	1440	288		5.0	.10 lb/shp
NACA Cyclogyro test result	NA	64		5.0	.15 lb /shp
Acuity modeled	960	80		12.0	.11 to .16 lb/shp*
Projected from Results	220	80		2.75	0.127
Projected from Results	457	80		5.71	0.183

Table 1. Performance of Several Helicopters and Predictions from NACA and Acuity Work

Therefore, the results obtained from our phase 1 tests indicate that a full size rotor with the same loading as a typical helicopter rotor can obtain comparable hover performance.

7.1.9.10 Parts Drawings

Drawings for the prototype cyclogyro rotor components are included at the end of this report.

7.1.9.11 Conclusions from Test Results

Cycloidal propulsion can be realized, and can be made practical for air vehicles. Many aspects of flight characteristics of a cyclogyro are beyond the scope of the Phase 1 work, but our results to date show significant promise for future work.

The aerodynamic characteristics of the rotor met or exceeded our expectations. The importance of precision part manufacturing and assembly and precise balancing were evident in our tests, as these ultimately limited the operating speed of the rotor. Stiffness in the central spar as well as the blades must be sufficient to keep resonant frequencies above operating speeds.

While the cyclogyro rotor suffers slight inefficiency in hover from the vertical motion of the blades and their inability to generate lift from that component of their motion, it has the advantage that the full length of the blade is moving at the same speed. Blade or rotor tip plates or airfoils may further increase efficiency over conventional rotorcraft. In forward cruise with the blades always oriented in the direction of travel the vertical motion will be less of a liability, since it will be less than the horizontal component from forward airspeed.

The cyclogyro has the additional potential advantages of low noise, high speed transport, and the ability to accelerate rapidly forward or backward from a hover. All of these would be significant improvements over current VTOL aircraft capabilities. These aspects of cycloidal propulsion make it an excellent candidate for military and civilian use, and warrant its continued study.

7.2 Future Technical Activities

We propose to continue this work in the following ways:

1. Develop blade angle profiles for a full range of airspeeds and methods of transitioning between them. Test this on the existing rotor.
2. Develop an adaptive blade angle algorithm which minimizes vibration and responds to airstream fluctuations while maintaining commanded lift, thrust and aircraft attitude and good propulsive efficiency. Test this on the existing rotor.
3. Modify the existing rotor and construct a second rotor and a scale model cyclogyro piloted by radio control. Test the results of 1-2 above on this aircraft. Demonstrate the feasibility of cycloidal propulsion for VTOL flight and a wide range of airspeeds.
4. Establish contacts with aircraft and powerplant manufacturers to develop business relationships based on design and construction of a manned cyclogyro prototype. Present the aircraft concept and test results to potential investors for phase III full scale development and test work.
5. Begin full scale design in cooperation with an aircraft manufacturer.

See our Phase II Proposal, submitted concurrently with this report, for a detailed description of future activities.

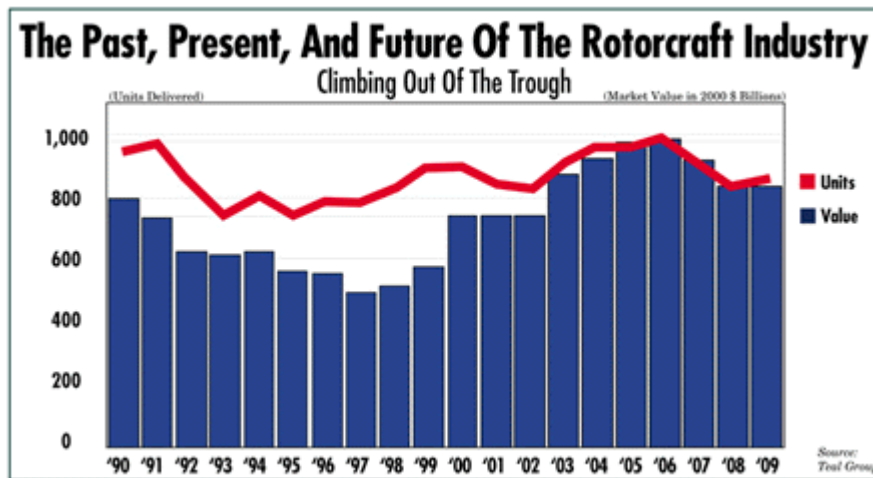
8 Potential Customer and Commercialization Activities

Since this project represents fundamental research, we have yet to initiate contact with potential customers and partners. That will be done in the phase 2 work. Acuity prefers to preserve the confidentiality of its work at this time.

8.1 Cumulative NASA Potential Customer Activities

8.2 Cumulative Non-NASA Potential Customer Activities

The market for VTOL rotorcraft is well quantified, as shown in the chart below. [21] The potential customers for the cyclogyro are actively purchasing rotorcraft, and demand will undoubtedly remain strong for the foreseeable future. The advantages in performance, safety, and sound levels that may be realized by the cyclogyro are



8.3 Other Cumulative Commercialization Activities

Acuity has filed a patent application based on concepts presented in the Phase 1 proposal. Future work will result in additional patent work to secure our interest in this technology.

Cyclogyros will be initially introduced in markets where the combination of vertical takeoff and landing, quiet operation, and high speed flight offer particular benefits. Potential initial markets include

Commercial:

Regional Air Transport: Scheduled flights, private aircraft, and fractional ownership.
Police and Coast Guard Rescue, Patrol and Interdiction

Defense:

Close Air and Ground Troop Support and Insertion, Removal
Search and Rescue
Reconnaissance
Transport
UAVs for any of the last 3.

Research:

Fundamental Aerodynamics of the Cyclogyro and Improvement of Flight Characteristics

9 Resources Status

All technical and other resources used in Phase 1 are employees and property of Acuity Technologies, and remain available for future work.

References

1. John B. Wheatley. "Simplified Aerodynamic Analysis of the Cyclogyro Rotating Wing System" NACA TN 467. Langley Memorial Aeronautical Laboratory, August 1933
2. John B. Wheatley and Ray Windler. "Wind Tunnel Tests of a Cyclogyro Rotor" NACA TN 528. Langley Memorial Aeronautical Laboratory, May 1935
3. Robinson Helicopter Company R22 Beta II Specifications, <http://www.robinsonheli.com/r22specs.htm>
4. Bell Helicopter, 407 specs, <http://www.bellhelicopter.textron.com/en/aircraft/commercial/prodSpecs407.cfm>
5. Dora Yen-Nakafuji "California Wind Resources", *Research and Development Office, Technology Systems Division, California Energy Commission. Presented at: Intra-state IEPR Workshop Sacramento, CA May 9, 2005*
6. Pershing, B. M. **Performance Prediction and Flight Evaluation of Hybrid Heavy Hift Systems.** AIAA-1986-2741 AHS, and ASEE, Aircraft Systems, Design and Technology Meeting, Dayton, OH, Oct. 20-22, 1986.
7. NASA NPARC Alliance, <http://www.arnold.af.mil/nparc/index.html>
8. M. A. Ramaswamy, "Characteristics of a Typical Lifting Symmetric Supercritical Airfoil", *Sadhana*, Vol 10 parts 3&4, pp 445-458. Presented at the 3rd Asian Congress on Fluid Mechanics, Tokyo, Sept 1986.
9. C. B. Strandgren, The Theory of the Strandgren Cyclogyro, NACA TM-727, Nov 1933. Translated from l'Aerophile, Vol. 41, No 7. July 1933.
10. Barnes W. McCormick *Aerodynamics, Aeronautics, and Flight Mechanics, 2nd Edition*, Wiley 1994
11. Dr. Konstantin Kovler, "Composite Materials" Technion, Division of Building Materials
12. Sigrafil GmBH Carbon composite products datasheet, www.sgcarbon.com/sgl_t/industrial/sigrafil/pdf/Sigrafil_e.pdf
13. Joseph E. Shigley *Mechanical Engineering Design*, McGraw-Hill, 1977
14. Robert M Rivello, *Theory and Analysis of Flight Structures*. McGraw-Hill, 1969
15. FlyingFoam core cutting, <http://www.flyingfoam.com/>
16. Compu-FoamCore, <http://www.compufoamcore.com/>
17. CST product site: <http://www.cstsales.com/CCCarbonFiberWrappedTubesIncludinG-Force.htm>
18. Airex Foam Specifications Sheet, <http://www.baltek.com/products/airex/airlite.html>
19. Kaydon Reali-slim bearings catalog, <http://www.reali-slim.com/pdfs/catalog300.pdf#page=15>
20. MicroPilot MP2028 datasheet, http://www.micropilot.com/prod_mp2028g.htm
21. http://www.aviationtoday.com/cgi/rw/show_mag.cgi?pub=rw&mon=1299&file=12rwoutlook.htm